



HAL
open science

Multi-Frequency Inversion of Ps and Sp Receiver Functions: Methodology and Application to USArray Data

Felix Bissig, Amir Khan, Benoit Tauzin, Paolo Sossi, Federico Munch, Domenico Giardini

► **To cite this version:**

Felix Bissig, Amir Khan, Benoit Tauzin, Paolo Sossi, Federico Munch, et al.. Multi-Frequency Inversion of Ps and Sp Receiver Functions: Methodology and Application to USArray Data. *Journal of Geophysical Research : Solid Earth*, In press, 10.1029/2020JB020350 . hal-03043029

HAL Id: hal-03043029

<https://hal.science/hal-03043029>

Submitted on 7 Dec 2020

HAL is a multi-disciplinary open access archive for the deposit and dissemination of scientific research documents, whether they are published or not. The documents may come from teaching and research institutions in France or abroad, or from public or private research centers.

L'archive ouverte pluridisciplinaire **HAL**, est destinée au dépôt et à la diffusion de documents scientifiques de niveau recherche, publiés ou non, émanant des établissements d'enseignement et de recherche français ou étrangers, des laboratoires publics ou privés.

1 **Multi-Frequency Inversion of Ps and Sp Receiver**
2 **Functions: Methodology and Application to USArray**
3 **Data**

4 **Felix Bissig¹, Amir Khan^{1,2}, Benoit Tauzin^{3,4}, Paolo A. Sossi⁵, Federico**
5 **D. Munch⁶, Domenico Giardini¹**

6 ¹Institute of Geophysics, ETHZ, Zürich, Switzerland

7 ²Institute of Theoretical Physics, University of Zürich, Zürich, Switzerland

8 ³Research School of Earth Sciences, ANU, Canberra, Australia

9 ⁴Université de Lyon, Université Claude Bernard Lyon 1, ENS, CNRS, Laboratoire de Géologie de Lyon:

10 Terre, Planètes, Environnement, Villeurbanne, France

11 ⁵Institute of Geochemistry and Petrology, ETHZ, Zürich, Switzerland

12 ⁶Department of Earth and Planetary Science, University of California, Berkeley, USA

13 **Key Points:**

- 14 • We describe a method for inverting multi-frequency P-to-s and S-to-p receiver func-
- 15 tions for mantle thermo-chemical structure
- 16 • We distinguish tectonic regions based on thermo-chemical characteristics across
- 17 the USA from the active West to the cratonic-orogenic East
- 18 • We observe strong thermo-chemically induced and interrelated topographic vari-
- 19 ations of the lithospheric base and the 410-km discontinuity

Abstract

We image the thermo-chemical structure of crust and mantle underneath the North American continent by inverting recordings of P-to-s (Ps) and S-to-p (Sp) converted seismic body waves (receiver functions; RF). Through careful data selection and processing, we construct a multi-frequency Ps (5, 8, 10 s) and Sp (10, 15 s) RF data set from USArray recordings. The inversion is interfaced with petrological phase equilibria computations to build self-consistent radial seismic velocity and density models for RF waveform simulations. Inverted models are combined through back-projection along converted ray-paths and interpolation to tomographic images of crust and mantle structure. Through clustering analysis we identify three major tectonic regions based on mantle thermo-chemical and seismic structure: the tectonically active West (TAW), the central transition regions (CTR), and the cratonic-orogenic East (COE). TAW is chemically more fertile with a $Mg\# \sim 0.90$ (molar $Mg\# = Mg/(Mg+Fe)$) and an elevated mantle potential temperature of 1490 ± 27 °C relative to COE, which is chemically more depleted ($Mg\# \sim 0.91$) and colder (1419 ± 27 °C). CTR is intermediate to TAW and COE. We find significant thermo-chemically-induced topography associated with the base of the lithosphere (± 90 km), while the mantle transition zone is mostly influenced by thermally-induced topography on the 410-km discontinuity (± 15 km). In contrast, the 660-km discontinuity, where variations are only ± 5 km, reflects a more complex thermo-chemical interplay. To place the results in a tectonic context, thermobarometric estimates from basaltic rocks across the western USA are integrated with the seismic inversions to produce a thermal model of the underlying mantle.

1 Introduction

Earth's thermal and compositional structure is the result of wide-ranging dynamical processes that have shaped and continue to shape the planet's surface and interior. Seismology provides tools for imaging traces of these processes, such as subducting slabs, thick continental roots, and mantle plumes, through their influence on material properties and thus seismic wave velocities and propagation.

These geologic features can be seismically imaged using converted, reflected, and refracted body waves (e.g. Farra & Vinnik, 2000; Flanagan & Shearer, 1998; Tan & Helmberger, 2007). For example, the construction of receiver functions (RFs) allows to extract timing and amplitude of P-to-s (Ps) and S-to-p (Sp) converted phases, which serve as proxy for imaging depth and sharpness of seismic discontinuities beneath a station, respectively (cf. Figure 1; Vinnik, 1977; Langston, 1979). Important seismic discontinuities include the base of the crust (Moho), the lithosphere-asthenosphere boundary (LAB), and the bounding discontinuities of the mantle transition zone (MTZ).

While the LAB primarily marks a change in thermal and rheological regime (e.g., Jaupart & Mareschal, 1999; Artemieva & Mooney, 2001; Eaton et al., 2009), two globally observable discontinuities bound the MTZ that are associated with the transformation of the mantle minerals olivine to wadsleyite and ringwoodite to bridgemanite+ferroperricline at depths of ~ 410 and ~ 660 km depth, respectively (Ringwood, 1975; Dziewonski & Anderson, 1981). The exact depth of these discontinuities (hereafter referred to as 410 and 660), is a non-linear function of local temperature, pressure, and composition (Bina & Helffrich, 1994; G. Helffrich, 2000; Xu et al., 2008). The RF technique serves as an excellent tool to study lateral thermo-chemically induced variations in discontinuity structure (e.g. Kumar et al., 2005; Lawrence & Shearer, 2006; Sodoudi et al., 2006; Andrews & Deuss, 2008; Tauzin et al., 2008; Geissler et al., 2010; Vinnik et al., 2010; Cottaar & Deuss, 2016; Knapmeyer-Endrun et al., 2017; Tauzin et al., 2017; Makushkina et al., 2019; Monna et al., 2019; Munch et al., 2020).

Here we consider Ps and Sp RFs to study crust, lithosphere, and mantle underneath the contiguous USA, which, from a geological point of view, offers a plethora of past and recent processes, encompassing areas from active tectonic regions in the west to precambrian and phanerozoic continental masses in the central and eastern parts (cf. Figure 2A–

73 B, Hoffman, 1989; Williams et al., 1991; Whitmeyer & Karlstrom, 2007; Mooney & Ka-
 74 ban, 2010). Seismic studies of the North American lithosphere, its base, and intra-lithospheric
 75 discontinuities have been considered extensively and provided insights into the processes
 76 that formed these complex continental entities (e.g., Rychert et al., 2007; H. Yuan & Ro-
 77 manovicz, 2010; Abt et al., 2010; H. Yuan et al., 2014; S. M. Hansen et al., 2015; Kind
 78 et al., 2015; Afonso et al., 2016; Calò et al., 2016; Eilon et al., 2018; Boyce et al., 2019;
 79 Kind et al., 2020). Seismic imaging of the mantle have tracked both recent (e.g., Juan
 80 de Fuca slab, Yellowstone plume) and ancient tectonic features (e.g., Farallon slab) (e.g.,
 81 van der Lee & Nolet, 1997; Burdick et al., 2008; Nettles & Dziewonski, 2008; Obrebski
 82 et al., 2010; Sigloch, 2011; Porritt et al., 2014; C. Chen et al., 2015; Maguire et al., 2018;
 83 Nelson & Grand, 2018; Krischer et al., 2018).

84 In this study, we aim to improve our current understanding of mantle structure and
 85 its relation to past and present dynamical processes underneath the North American con-
 86 tinent by providing a more detailed view of the combined thermo-chemical structure of
 87 Moho, LAB, upper mantle, and MTZ. For this purpose, we will build upon and extend
 88 the work of Munch et al. (2018), who combined mineral phase equilibrium computations
 89 with geophysical inversion to self-consistently image the thermo-chemical structure of
 90 the MTZ using P-to-s waves converted at the 410 (P410s) and 660 (P660s). There are
 91 several advantages to this approach in that it anchors temperature, composition, seis-
 92 mic properties, and discontinuities that are in laboratory-based forward models, while
 93 simultaneously permitting, through inversion, to optimize profiles of physical properties
 94 (e.g., S-wave velocity) to match seismic data.

95 We consider a number of improvements and extensions to our previous work by 1)
 96 including Sp RFs; 2) considering multiple frequency bands for both Ps and Sp RFs; and
 97 3) applying the methodology to USArray data to perform a tomographic study of the
 98 North American continent. Points 1) and 2) allow for significant improvement in reso-
 99 lution of lithosphere, upper mantle, and transition zone structure. With these improve-
 100 ments in place, we are able to identify three major tectonic provinces based directly on
 101 differences in mantle thermo-chemical and seismic structure that show significant thermo-
 102 chemically induced variations across the LAB and MTZ. We further observe well known
 103 tectonic features in our tomographic images, such as hot mantle upwelling underneath
 104 the western USA as well as traces of active and ancient subduction.

105 This paper is divided into two parts: a methodological and an application part. In
 106 part 1 (sections 2–3), we describe seismic data processing to construct a new set of multi-
 107 frequency Ps and Sp RFs using USArray data with particular emphasis on Sp RFs (Ps
 108 RFs are detailed in Munch et al. (2018)), including data selection, deconvolution, spa-
 109 tial sensitivity analysis, stacking and uncertainty estimation, and RF modeling as part
 110 of which we perform a benchmark of one-dimensional (1-D) synthetic waveforms against
 111 three dimensional (3-D) full waveform synthetics to validate our 1-D modeling approach
 112 to computing seismograms. In part 2 (sections 4–7), we apply the developed method-
 113 ology to obtain self-consistent tomographic images of the crust, lithosphere, and man-
 114 tle underneath the North American continent. Part 2 includes model parametrization,
 115 inversion procedure, and discussion of results. Finally, to further test the results presented
 116 here, we compare our thermal model with an independent model of the western USA con-
 117 structed from thermobarometry data.

118 2 Data processing

119 The fundamental idea of the receiver function method is to separate signals gen-
 120 erated by the direct and converted phases on three-component ground-motion record-
 121 ings based on their distinct particle motion (e.g., Rondenay, 2009; Kind et al., 2012). In
 122 the case of a P-to-s conversion, the P-motion is recorded on the vertical component and
 123 the converted wave on the radial component, while the order is reversed for S-to-p con-
 124 versions. The converted signal can be considered as the convolution of the direct wave-
 125 field with the local structural response. Thus, deconvolving the “source”- (i.e., direct phase)

126 from the “response”-trace (i.e., converted phase) results in a time series representing the
 127 structure below the receiver. This time series is called the receiver function (cf. Figure 1B–
 128 C; Vinnik, 1977; Langston, 1979). Source and path effects between event and conver-
 129 sion point are assumed to be removed through the deconvolution operation, as all this
 130 information is contained in both, source- and response-traces (Kind et al., 2012).

131 In spite of certain advantages of Sp over Ps RFs, the use of the former for mak-
 132 ing structural inferences is limited relative to the latter because of limitations that be-
 133 set S-waves (e.g., Bock, 1994; Farra & Vinnik, 2000; X. Yuan et al., 2006; Wilson et al.,
 134 2006). Firstly, the incidence angle of S-to-p converted phases is larger than that of the
 135 original S-wave, causing post-critical incidence to restrict the usage of Sp RFs to nar-
 136 rower epicentral distance ranges and depths shallower than 660 km (cf. Figure 1A). Also,
 137 because of the large incidence angle, S-to-p conversion points are located farther away
 138 from the station than in the case of P-to-s, which ultimately results in broader regional
 139 sampling. Added to this, is a lower spatial resolution because of a lower frequency con-
 140 tent of S-waves relative to P-waves. Secondly, the signal-to-noise ratio (SNR) of S-waves
 141 is lower than for P-waves because of a range of interfering phases, which generally com-
 142 plicates observation of S-to-p converted phases. In this context, Bock (1994) and Wilson
 143 et al. (2006) have pointed out that amplitudes of P-wave multiples between the surface
 144 and the MTZ can become significant to the extent that these can be mistaken for con-
 145 versions. Thirdly, core-phases (ScS, SKS, and their respective conversions) in the epi-
 146 central distance range $\sim 85^\circ$ – 100° interfere with S-to-p conversions, in particular S660p
 147 phases (X. Yuan et al., 2006). These issues can, however, to a large extent be mitigated
 148 through careful data selection and processing steps as described in e.g., Wilson et al. (2006);
 149 Monna et al. (2019); X. Shen et al. (2019).

150 2.1 Data selection

151 We collected and processed data recorded at stations of the USArray (Figure 2C),
 152 which includes about 100 reference stations in complementary use to the denser trans-
 153 portable network. Seismic data were acquired from the IRIS datacenter (Incorporated
 154 Research Institutions for Seismology, ds.iris.edu/ds/nodes/dmc/) using ObspyDMT
 155 (Hosseini & Sigloch, 2017). Event selection is based on information available from the
 156 global centroid moment tensor catalogue (Dziewonski et al., 1981; Ekström et al., 2012,
 157 www.globalcmt.org). Only events with a magnitude of at least 5.5 and a focal depth
 158 shallower than 150 km were selected. The latter criterion is applied to reduce the inter-
 159 ference of S-to-p conversions with surface-reflected multiples (Wilson et al., 2006). For
 160 constructing Ps RFs, we select events in the epicentral distance (Δ) range 40° – 95° (e.g.,
 161 Andrews & Deuss, 2008). For Sp RFs, we are restricted to a Δ range of 55° – 90° because
 162 of post-critical incidence. Also, because of the simultaneous arrival of SKS and ScS (in-
 163 cluding their conversions) beyond 85° , the S660p conversion is very difficult to observe
 164 (X. Yuan et al., 2006). We therefore focus on S-to-p conversions at discontinuities be-
 165 tween the Moho and the 410. The selected distance ranges and the respective travel times
 166 of direct and converted waves are shown in supplementary Figure S.1.

167 2.2 Receiver function processing

168 For each event, recordings are filtered between 0.02 Hz and 1 Hz using a Butter-
 169 worth bandpass filter of 2nd order and then rotated to the ZRT (vertical-radial-transverse)
 170 system under consideration of the back-azimuth computed from the source and receiver
 171 locations. In the Sp case, we additionally rotate waveforms to the LQT-system, where
 172 the orthogonal L and Q components are approximately aligned with the S and S-to-p
 173 converted phases, respectively, improving their detectability (Rondenay, 2009; Kind et
 174 al., 2012). The orientation of the L- and Q-axes is determined by maximizing the en-
 175 ergy in the window from -30 s to +50 s on the Z-/L-component around the theoretical
 176 S-wave arrival by means of principal component analysis (PCA; see supplementary Fig-

177 ure S.2). In order to determine the SNR and exact arrival of the direct phase, we im-
 178 plemented the automated picking approach of Abt et al. (2010). An illustration hereof
 179 is shown in supplementary Figure S.3. To ensure high-quality data, we only consider wave-
 180 forms with a $\text{SNR} > 5$. Alternative SNR criteria for detecting lithospheric S-to-p conver-
 181 sions have also been proposed by X. Shen et al. (2019) and Monna et al. (2019).

182 **2.2.1 Deconvolution**

183 Receiver functions are obtained from deconvolving source (direct phase) from re-
 184 sponse waveform (converted phase). The source wavelet is extracted by trimming the
 185 corresponding trace around the picked arrival of the direct phase within windows from
 186 -50 s to +150 s and from -100 s to +30 s for Ps and Sp RFs, respectively. Analogously,
 187 the response trace is cut within a window from -50 s to +150 s and from -150 s to +50 s
 188 for Ps and Sp RFs, respectively. The tapered source and response waveforms are sub-
 189 sequently deconvolved using iterative time-domain deconvolution (Ligorria & Ammon,
 190 1999). For removing high-frequency noise from the RFs, a Butterworth lowpass filter of
 191 2nd order is applied for different corner periods: 5 s, 8 s, and 10 s for Ps RFs and 10 s
 192 and 15 s for Sp RFs. This choice is dictated by the increased noise-content at shorter
 193 periods and lack of resolution at longer periods, respectively. Maximum wavelengths as-
 194 sociated with these periods are 28–56 km for Ps and 90–135 km for Sp RFs, respectively.
 195 Since the arrival times of converted phases not only depend on the structure below the
 196 receiver but also on the slowness of the ray, we stretch and compress the time axis of each
 197 RF to a reference slowness (moveout correction), that is 6.5 s/° for Ps RFs and 9.9 s/°
 198 for Sp RFs. For comparison with Ps RFs, the time axis and polarity of Sp RFs are flipped.

199 **2.2.2 Stacking and uncertainty estimate**

200 To further enhance SNR, we stack individual RF traces at a given station. This
 201 ensures that information from many events, where focal depth, mechanism, and epicen-
 202 tral distance differ, are combined coherently. Phases not aligned through the moveout
 203 correction are cancelled and hence direct conversions enhanced. To determine uncertain-
 204 ties on RFs, we employ a bootstrap resampling approach (Efron & Tibshirani, 1991) and
 205 compute the standard deviation of 100 stacks, where each stack is formed from n ran-
 206 domly recombined RFs, with n being the number of available RF traces. A crucial choice
 207 has to be made on the selection of RF traces to be included in a stack, as this depends
 208 on the spatial sensitivity of the data set, i.e., location of conversion points relative to sta-
 209 tion and frequency content.

210 **2.2.3 Spatial sensitivity of Sp RFs**

Assuming the main sensitivity of a RF to be confined to the region directly beneath
 the station allows us to sum all moveout-corrected RF traces available to form a stack.
 While this assumption is reasonable for P-to-s conversions and therefore applied to the
 Ps RF data set, it is not directly applicable to the S-to-p conversions, because of the high
 incidence angles compared to the direct S-wave. Consequently, S-to-p conversion points
 are located significantly further away from the station than those of P-to-s converted waves
 from the same depth (cf. Figure 1A). Moreover, S-to-p converted waves propagate faster
 and hence have longer wavelengths. These effects are illustrated for Sp RFs obtained at
 station 39-COWI (‘39’ referring to the station-ID in Figure 2C and ‘COWI’ being the
 station-abbreviation) and filtered at 10 s period by computing and plotting the Fresnel
 volumes of converted waves at different depth slices following the approaches of Lekic
 et al. (2011) and Cottaar and Deuss (2016). For each event present in the Sp RF data
 set for station 39-COWI, we 1) determine S-to-p conversion points at depth Z using ray-
 tracing through IASP91 (Kennett & Engdahl, 1991; Crotwell et al., 1999), and 2) com-
 pute the Fresnel zone half-width, δ^{HW} , at the same depth Z , which is a function of wave-

length, λ , via:

$$\delta^{\text{HW}} = \sqrt{\left(\frac{\lambda}{3} + Z\right)^2 - Z^2} \quad (1)$$

where λ is obtained by multiplying the P-wave velocity above Z , i.e., the velocity of the converted wave, with the dominant period (here 10 s). Knowing the location of conversion points and Fresnel zones, we evaluate the lateral sensitivity of the ray by comparing δ^{HW} for each node on a discrete grid at distance δ to the conversion point of interest via normalized cubic splines:

$$w = \begin{cases} \frac{3}{4}\bar{\delta}^3 - \frac{3}{2}\bar{\delta}^2 + 1, & \text{if } \bar{\delta} \leq 1 \\ \frac{1}{4}(2 - \bar{\delta})^3, & \text{if } 1 < \bar{\delta} \leq 2 \\ 0, & \text{if } \bar{\delta} \geq 2 \end{cases} \quad (2)$$

211 where $\bar{\delta} = \delta/\delta^{\text{HW}}$. We performed this analysis for conversions at 210 km and 410 km
 212 depth (see Figure 3A–B). The weights of all rays included in a certain back-azimuth bin
 213 are summed and re-scaled by the maximum value to facilitate comparison. Note that the
 214 width of the Fresnel volume is not the resolution limit of a seismic wave (Spetzler & Snieder,
 215 2004), but serves as a useful illustration of the latter.

216 For station 39-COWI, we observe that the group of events emanating from the west-
 217 ern Pacific, South America, and Europe (Figure 3E) produce distinct sensitivity clus-
 218 ters at 210 km and 410 km depth (Figure 3A–B). Their clear separation indicates that
 219 summing RFs from the entire data set would lead to averaging of lithospheric and up-
 220 per mantle structure from different regions. Instead, it requires forming stacks that are
 221 sorted by back-azimuth (e.g., Vinnik et al., 2005; Vinnik et al., 2010; Monna et al., 2019).
 222 However, back-azimuth binned stacks reduce the number of useful traces available in one
 223 back-azimuth bin to between 10 and 80; yet, Sp RF stacks containing less than ~ 100
 224 traces tend to be noisy and, consequently, less robust (see supplementary section S.2).
 225 A possible work-around is to increase the number of traces within a back-azimuth bin
 226 by incorporating additional data as shown in the following.

227 **2.2.4 Back-azimuth stacking using additional stations**

228 In addition to the reference network (Figure 2C), USArray also consists of a dense
 229 network of transportable stations. Since stations are only spaced about 60 km apart, events
 230 of similar back-azimuth recorded at neighbouring stations will produce S-to-p converted
 231 waves that sample a similar region as illustrated in Figure 3C–D. Thus, the amount of
 232 data in a back-azimuth bin for a given reference station can be increased by including
 233 data recorded at near-by transportable stations.

234 This is illustrated in Figure 4 for the reference station 39-COWI, which shows how
 235 the uncertainty and amplitudes of the Sp RF stack evolve as traces from the transportable
 236 stations closest to 39-COWI are added for events in the western Pacific (back-azimuth
 237 bin #1, panels A and B) and Europe (back-azimuth bin #3, panels C and D), respec-
 238 tively. For both back-azimuth clusters, we see that the bootstrap-derived mean uncer-
 239 tainty of the cumulative stack decreases and that RF amplitudes change when the num-
 240 ber of traces is increased. The improvement in the quality of the Sp RF is particularly
 241 evident in the case of the S410p phase that emerges in back-azimuth bin #3, which is
 242 far less apparent in the Sp RF 39-COWI-only stack. Although the final number of traces
 243 used (~ 50) for this particular event cluster remains below the threshold associated with
 244 a robust stack, back-azimuth bin #1 includes more than 150 traces. In combination with
 245 the clear signals emanating from Moho, lithosphere, and the 410-km discontinuity, we
 246 therefore consider this to be a high-quality stack and retain it for the inversion.

247 An alternative approach would be common-conversion point (CCP) stacking, which
 248 migrates each individual RF trace from time- to depth-domain according to its conver-
 249 sion points (e.g., Dueker & Sheehan, 1997; Kosarev et al., 1999; Rondenay, 2009; Lekić
 250 et al., 2011; Lekić & Fischer, 2014; Cottaar & Deuss, 2016; Lekić & Fischer, 2017; Kind

et al., 2020). This method, however, depends crucially on the background velocity model used for migration and, unless data are properly re-processed during inversion using the currently updated velocity model, is not self-consistent and therefore limited in accuracy.

2.3 Data workflow summary

We processed Ps and Sp RFs for all USArray reference stations (Figure 2C). This included the following steps:

- Construction of a multi-frequency Ps (5, 8, and 10 s low-pass period) and Sp (10 and 15 s low-pass period) RF data set.
- Formation of Sp RF stacks sorted by back-azimuth by combining data recorded at USArray reference and transportable stations that are located at a maximum distance of 140 km from the former.
- Selection of robust and only highest quality Ps and Sp RFs with clear signals emanating from the Moho, lithosphere, 410, and 660 for the inversion (cf. Table S.1 in the supplementary material).

3 Synthetic receiver function modeling

In order to generate a synthetic RF stack equivalent of the observed RF stack, we first compute waveforms using the reflectivity method (Fuchs & Müller, 1971; Müller, 1985). In order to ensure consistency, synthetic waveforms are processed the same way as the observed data (Munch et al., 2018). For optimal radiation of P and SV waves, we model the source as an explosion for Ps RFs and a normal-fault mechanism for Sp RFs. The source-time function is a Heaviside function and the modeled focal depth is imposed by the median of the depth distribution of the observed events. As the amplitudes of converted waves depend on slowness, their relative contribution to the final RF stack has to be mimicked in the synthetic RF modeling. The distribution of receivers and their relative weights in the stack therefore follows that of the distribution of the theoretical slownesses of the direct phase as imposed by the data set (Munch et al., 2018).

We exclude the uppermost layer of the model from the reflecting zone when computing waveforms for Sp RF (cf. supplementary Figure S.6). This suppresses multiple surface reflections which otherwise would constructively interfere and bias the RF. This approach is similar to the one by X. Yuan et al. (2006), who argue that propagation of multiples in a laterally heterogeneous Earth is ineffective. Ultimately, synthetic waveforms also have to conform to the following criteria: 1) the L- and Q-axis as imposed by the data set are employed to ensure consistency between observed and synthetic LQT-systems, since these affect RF amplitudes, and 2) the arrival time of the direct phase for the underlying model is determined via ray tracing (Crotwell et al., 1999), since the automated picking algorithm is unable to distinguish core phases from S-waves for $\Delta > 85^\circ$.

Finally, in order to validate our one dimensional (1-D) modeling approach to computing synthetic seismograms, we benchmarked the modeled receiver functions against three dimensional (3-D) full waveform synthetics (see supplementary section S.3.2). For this purpose, we employed the spectral element based software package Salvus (Afanasiev et al., 2019) to compute full waveforms in a 3-D velocity model. Comparison of 1-D and 3-D receiver functions is shown in supplementary Figure S.7 and the modeled waveforms are seen to be in good agreement. On the basis of this benchmark, the 1-D approach pursued here appears to be reliable for modeling both, Ps and Sp RFs, and, from a practical viewpoint, computationally much more efficient (1-D: ~ 15 – 20 sec on a normal desktop-computer, 3-D: ~ 25 nodehours on a supercomputer).

4 Model parametrization

4.1 Petrological model

Building on previous experience (e.g., Khan et al., 2009; Munch et al., 2018), we model mantle composition by the weight fraction of basalt in a basalt-harzburgite mixture. This compositional model is based on the recognition that basaltic crust is generated at ridges through partial melting, leaving behind the depleted complement harzburgite (Xu et al., 2008). At subduction zones, this physically and chemically stratified oceanic lithosphere is continuously being recycled back into the mantle, where it remixes (e.g., G. R. Helffrich & Wood, 2001; Tackley et al., 2005). The resultant mineralogy depends on the degree of equilibration between basalt and harzburgite and two mixing models have been proposed (Xu et al., 2008): equilibrium assemblage (EA) and mechanical mixture (MM). The EA model assumes full equilibration, whereas in the MM model the mantle is a mixture of the end-members. Here, we focus on the EA model as Munch et al. (2018) have shown that RFs are less sensitive to differences between MM and EA.

For a given basalt fraction f , mantle composition \mathbf{X} is computed from

$$\mathbf{X} = f\mathbf{X}_B + (1 - f)\mathbf{X}_H, \quad (3)$$

where \mathbf{X}_B and \mathbf{X}_H are basaltic and harzburgitic end-member compositions, respectively. To predict the relative amount of stable minerals and their physical properties along a self-consistent mantle adiabat for harzburgite and mid-ocean ridge basalt (MORB) bulk chemical compositions in the $\text{Na}_2\text{O}-\text{CaO}-\text{FeO}-\text{MgO}-\text{Al}_2\text{O}_3-\text{SiO}_2$ system (Table 1), we employ Gibbs free energy minimization and equation-of-state modeling (Perple_X; Connolly, 2009). For this purpose, we adopt the thermodynamic formulation of Stixrude and Lithgow-Bertelloni (2005) and parameters and uncertainties as given by Stixrude and Lithgow-Bertelloni (2011). Bulk rock properties are subsequently obtained by means of Voigt-Reuss-Hill averaging (Hill, 1952; Watt et al., 1976). Density and elastic moduli are accurate to within $\sim 0.5\%$ and $\sim 1-2\%$, respectively (Connolly & Khan, 2016). To obtain the mantle pressure profile, we integrate the vertical load from the surface pressure boundary condition. Within the crust and lithosphere, temperature is computed by assuming a conductive geothermal gradient, while the sublithospheric mantle adiabat is defined by the entropy of the lithology at the base of the lithosphere (see supplementary Figure S.8 for an illustration).

The present thermodynamic model of Stixrude and Lithgow-Bertelloni (2005, 2011) has limitations: 1) the equilibrium assumption is dubious at low temperatures as equilibrium is not likely to be achieved (e.g., Wood & Holloway, 1984). Consequently, we compute mineralogy for temperature below 500°C at 500°C , and the resultant mineralogy is then used to calculate physical properties at the temperature of interest; and 2) the thermodynamic model does not account for redox effects (e.g., Cline II et al., 2018), minor phases, and water and melt due to lack of thermodynamic data. Both, water and melt, can significantly affect elastic properties at lithospheric and MTZ depth. Negative gradients in S-wave velocity ($> 5\%$) at mid-lithospheric depth in continental regions could arise from hydrous minerals (D. H. Green et al., 2010; Rader et al., 2015; Selway et al., 2015) and low wave velocities at the lithosphere-asthenosphere boundary in oceanic and active regions have been attributed to partial melt (e.g., Kawakatsu et al., 2009; Rychert & Shearer, 2009; Lekić & Fischer, 2014; Stern et al., 2015; Clark & Leshner, 2017; Karato & Park, 2019). The MTZ is considered as a plausible water reservoir within the mantle given the experimentally constrained storage capacities (1-3%) of wadsleyite and ringwoodite (Smyth, 1987; Kohlstedt et al., 1996; Férot & Bolfan-Casanova, 2012). However, mineral physics data suggest the effect of water on seismic velocities is negligible at MTZ conditions as a result of which seismic data are insensitive to water content (Thio et al., 2015; Schulze et al., 2018). Albeit, there is geophysical evidence for regional low-velocity layers atop the 410 (e.g., Song et al., 2004; Toffelmier & Tyburczy, 2007; Vinnik & Farra, 2007; Tauzin et al., 2010; Khan & Shankland, 2012; Kind et al., 2015; Xiao

Table 1. Model mantle compositions in wt% of mid-ocean ridge basalt (MORB) and its depleted residue, harzburgite (from Khan et al. (2009)). Mg# (molar) is given by $\text{Mg}/(\text{Mg} + \text{Fe})$.

Component	MORB, \mathbf{X}_B	Harzburgite, \mathbf{X}_H
CaO	13.05	0.5
FeO	7.68	7.83
MgO	10.49	46.36
Al ₂ O ₃	16.08	0.65
SiO ₂	50.39	43.64
Na ₂ O	1.87	0.01
Mg#	0.709	0.913

348 et al., 2020), which might be due to partial melt (Bercovici & Karato, 2003; Hirschmann,
 349 2006; Freitas et al., 2017). Future studies will consider this in more detail.

350 4.2 Crustal structure

351 The velocity structure of the crust is important for modeling receiver functions (see
 352 supplementary sections S.5.1 and S.5.3.2). Here, we follow Munch et al. (2018) and model
 353 the crust as a stack of three layers of variable thickness and S-wave velocity, which is as-
 354 sumed to increase with depth. The ratios of density and P-wave velocity to S-wave ve-
 355 locity are constant in the crust. We invert for all of these parameters by using conver-
 356 sions at the Moho and P-to-s crustal reverberations.

357 4.3 Anelastic effects

358 In order to model the effect of anelasticity on seismic amplitudes (Liu, 2003), we
 359 follow the scheme outlined in Munch et al. (2018), which considers a laboratory-based
 360 viscoelastic dissipation model derived from grain-size-, temperature-, and pressure-sensitive
 361 viscoelastic relaxation measurements. The dissipation model based on the extended Burg-
 362 ers model is described in detail in Jackson and Faul (2010) and relies on laboratory ex-
 363 periments in the temperature range 800–1200 °C of torsional forced oscillation data within
 364 1–1000 s period on melt-free poly-crystalline olivine grains between 3–165 μm size. Ra-
 365 dial profiles of shear attenuation, Q_μ , are determined for the viscoelastic extended Burg-
 366 ers model using the implementation of Bagheri et al. (2019), for which rheological pa-
 367 rameters are listed in supplementary Table S.2.

368 The advantage of this particular set-up is that it allows us to account for, through
 369 the thermodynamic interface, the influence of temperature and pressure on the shear at-
 370 tenuation model in a self-consistent manner (e.g., Bagheri et al., 2019). Alternative vis-
 371 coelastic models have also been proposed (e.g., Jackson & Faul, 2010; Sundberg & Cooper,
 372 2010; Karato et al., 2015), but the relatively high-frequency Ps and Sp RFs are not sen-
 373 sitive enough to allow for proper discrimination (see discussion in supplementary sec-
 374 tion S.6.3). In case Q_μ exceeds 600, Q_μ is set equal to 600 and bulk attenuation, Q_κ , is
 375 held fixed at 57823 after PREM (Dziewonski & Anderson, 1981).

376 5 Inverse problem

377 5.1 Formulation of the inverse problem

Within the Bayesian framework, the solution to the inverse problem $\mathbf{d} = \mathbf{g}(\mathbf{m})$,
 where \mathbf{d} is a data vector containing observations and \mathbf{g} a typically non-linear operator

Table 2. Overview of model parameters, their quantity, and prior model parameter ranges and probability distributions

Description	Parameter	Quantity	Value/range	Distribution
Basalt fraction	f	1	0–0.5	uniform
Lithospheric temperature (°C)	T_{lit}	1	950–1600	uniform
Lithospheric thickness (km)	Z_{lit}	1	70–300	uniform
Crustal layer thicknesses (km)	δZ	3	1–20	uniform
S-wave velocity of uppermost crustal layer (km/s)	V_S^1	1	2.0–4.1	uniform
S-wave velocity change across crustal discontinuities (km/s)	δV_S	2	0–0.5	uniform
Density- and P-to-S-wave velocity crustal ratios	ρ/V_S V_P/V_S	1 1	0.768 ± 0.0213 1.746 ± 0.0195	normal normal

that maps a model parameter vector \mathbf{m} into data, is given by (Mosegaard & Tarantola, 1995)

$$\sigma(\mathbf{d}, \mathbf{m}) = k \cdot h(\mathbf{m})\mathcal{L}(\mathbf{d}, \mathbf{m}), \quad (4)$$

378 where k is a normalization constant, $h(\mathbf{m})$ is the prior probability distribution on model
379 parameters (see Table 2) and contains information about model parameters obtained in-
380 dependently of the data under consideration, $\mathcal{L}(\mathbf{d}, \mathbf{m})$ is the likelihood function, which
381 can be interpreted as a measure of misfit between the observations and the predictions
382 from model, and $\sigma(\mathbf{d}, \mathbf{m})$ is the posterior model parameter distribution containing the
383 solution to the inverse problem. The particular form of $\mathcal{L}(\mathbf{d}, \mathbf{m})$ is determined by the ob-
384 servations, their uncertainties, and model data noise and will be discussed in the follow-
385 ing section.

386 5.2 Definition of the likelihood function

We only consider the time windows that include Ps and Sp RF signal of interest, i.e., converted energy from the Moho (and reverberations thereof), the 410, and the 660 for Ps RFs, and the Moho, the lithosphere, and the 410 for Sp RFs. The windows are determined manually for each stack as illustrated in Figure 5 (gray areas). For each window i , observed RF, and low-pass period T , we consider a L_2 -based likelihood function of the form

$$\mathcal{L}_{T,i}^{\text{RF}}(\mathbf{d}, \mathbf{m}) = \exp(-\Phi_{T,i}^{\text{RF}}), \quad (5)$$

where

$$\Phi_{T,i}^{\text{RF}} = \frac{1}{N} \sum_j \frac{\|\mathbf{d}_j^{\text{obs}} - \mathbf{d}_j^{\text{syn}}\|^2}{2\sigma_j^2} \quad (6)$$

with $\mathbf{d}_j^{\text{obs}}$, $\mathbf{d}_j^{\text{syn}}$, and σ_j being synthetic and observed Ps or Sp RF amplitudes (for a given period and window) and data uncertainty of data point j , respectively, with N denoting the total number of points within each misfit window. Consequently, the total likelihood function for a given station, RF-type, and back-azimuth bin is the conjunction of the likelihood functions associated with each period and misfit window:

$$\mathcal{L}(\mathbf{d}, \mathbf{m}) = \prod_{T,i} \mathcal{L}_{T,i}^{\text{RF}}(\mathbf{d}, \mathbf{m}) \quad (7)$$

387 5.3 Sampling of the posterior

We sample the posterior distribution by means of the Metropolis-Hastings algorithm (Metropolis et al., 1953; Hastings, 1970). This algorithm is based on random sam-

pling of the model space, yet only models that result in a good data fit and are consistent with prior information are frequently sampled (importance sampling). At each step n , a model, \mathbf{m}^{n+1} , is proposed on the basis of the prior distribution and is either accepted or rejected based on the probability

$$P = \min \left[1, \frac{\mathcal{L}(\mathbf{m}^{n+1})}{\mathcal{L}(\mathbf{m}^n)} \right], \quad (8)$$

where \mathbf{m}^n represents the last accepted model. In a slight modification, we use the cascaded Metropolis algorithm (Mosegaard & Tarantola, 1995, 2002), which applies the acceptance criterion (Eq. 8) to each period T and misfit window i (crust, lithosphere, 410, and 660) separately for a given station and individual RF-type (and back-azimuth bin):

```

388 where  $\mathbf{m}^n$  represents the last accepted model. In a slight modification, we use the cas-
389 caded Metropolis algorithm (Mosegaard & Tarantola, 1995, 2002), which applies the ac-
390 ceptance criterion (Eq. 8) to each period  $T$  and misfit window  $i$  (crust, lithosphere, 410,
391 and 660) separately for a given station and individual RF-type (and back-azimuth bin):
392
393   (*) propose move:  $\mathbf{m}_{\text{RF}}^n \rightarrow \mathbf{m}_{\text{RF}}^{n+1}$  RF=Ps or RF=Sp
394   for  $T = 5, 8, 10$  s (if RF=Ps) /  $10, 15$  s (if RF=Sp)
395     for  $i = 1, 2, 3$ 
396       if  $\mathcal{L}_{T,i}^{\text{RF}}(\mathbf{m}_{\text{RF}}^{n+1}) \geq \mathcal{L}_{T,i}^{\text{RF}}(\mathbf{m}_{\text{RF}}^n)$  then
397         accept this step
398       else if  $\mathcal{L}_{T,i}^{\text{RF}}(\mathbf{m}_{\text{RF}}^{n+1}) < \mathcal{L}_{T,i}^{\text{RF}}(\mathbf{m}_{\text{RF}}^n)$  then decide randomly to move to
399         the next step or to reject the proposed move with probability
400          $P = \mathcal{L}_{T,i}^{\text{RF}}(\mathbf{m}_{\text{RF}}^{n+1}) / \mathcal{L}_{T,i}^{\text{RF}}(\mathbf{m}_{\text{RF}}^n)$ 
401       else reject  $\mathbf{m}_{\text{RF}}^{n+1}$  and return to (*)
402     end
403   end

```

Thus, the model is only retained if all of the individual steps are accepted. This acceptance criterion is more strict when compared to the “standard” acceptance criterion of the Metropolis-Hastings algorithm, but acts to prevent trade-offs between misfit windows as these are considered separately.

Finally, to improve MCMC performance, we reduced the burn-in of the sampling stage by employing a global optimisation method in order to obtain a good initial model for the subsequent model space search. For this purpose, we use the Covariance Matrix Adaption Evolution Strategy of Hansen and Ostermeier (2001). We first search for a crustal model by minimizing the misfit in the crustal time window, and subsequently refine both crustal and thermo-chemical model by minimizing misfit across all windows. In the MCMC stage, we sampled ~ 40000 models in total by running 8 chains in parallel, of which ~ 4000 models are retained for analysis here. Step lengths are adjusted so that the acceptance rate is between 30–50%. Synthetic test inversions and grid-search examples are described in the supplementary section S.5.

5.4 A posteriori migration of inversion results

We created a series of maps and cross sections to visualize the spatial variation of model parameters based on mean models. The use of mean models is justified given that the posterior probability density distributions (Figure 6) are mostly Gaussian. Maps and cross sections are produced through linear interpolation of the Ps and Sp RF-derived mean models, which were migrated to their point of sensitivity, which, in the case of Ps RFs, is approximately the location of the station and for Sp RFs is the conversion point of the Sdp phase (cf. section 2.2.3), where d is the depth of sensitivity of a particular model parameter. For example, when migrating Sp RF-derived crustal and lithospheric thickness, d equals either Z_c or Z_{lit} , whereas in the case of temperature, d is equal to 410 km, since thermal information is primarily contained in the S410p phase (see supplementary Figure S.15).

For a given station, back-azimuth bin, and model parameter with sensitivity d , we compute the coordinates of the Sdp conversion points in IASP91 for all events included in that bin and average them to extract the final point of sensitivity. The so-computed Sp RF points are shown as diamonds in the maps that follow, while Ps RF points, i.e., station locations, are depicted as circles. All estimates related to discontinuity structure

434 (Moho, LAB, and MTZ) have been corrected for station elevation. Finally, while the present
 435 inversion is not a tomographic inversion *sensu stricto*, it is an inversion for a set of (quasi-
 436 local) radial profiles of thermochemical and physical structure, which, when pieced to-
 437 gether, result in tomographic images that are based on the a posteriori migration pro-
 438 cedure.

439 6 Results and Discussion

440 6.1 Datafit

441 The fits to observed Ps and Sp RFs at 5 and 10 s period, respectively, are shown
 442 in Figure 5. Fits to Ps and Sp RFs at the other periods are summarised in supplemen-
 443 tary Figure S.19. Conversions at the Moho, 410, and 660 discontinuities as well as litho-
 444 spheric Sp RFs are seen to be captured well by the sampled models.

445 6.2 Crustal thickness

446 The inverted mean crustal thickness model is shown in Figure 7A. Results for ρ/V_S
 447 and V_P/V_S can be found in the supplementary material (Figure S.20). The abbrevia-
 448 tions and extent of physiographic and tectonic provinces referred to hereafter are depicted
 449 in Figure 2A–B. As expected, crustal thickness estimates are better constrained from Ps
 450 than from Sp RFs (Figure 6A–B) given the higher frequency content of Ps RFs and the
 451 additional information contained in crustal reverberations. Mean Ps and Sp RF derived
 452 standard deviations are 1.6 km and 3.5 km, respectively. For comparison, we are also
 453 showing the crustal thickness map based on Crust1.0 (Laske et al., 2013) in Figure 7B.
 454 Our model is in good agreement with Crust1.0, including other models (not shown; e.g.,
 455 Lowry & Pérez-Gussinyé, 2011; Levander & Miller, 2012; Schmandt et al., 2015; W. Shen
 456 & Ritzwoller, 2016; Buehler & Shearer, 2017; Ma & Lowry, 2017) which indicate that
 457 regions with relatively thin crust (25–35 km) are found in the western part of the USA,
 458 i.e., beneath the Columbia plateau (physiographic province P2) and the Basin and Range
 459 province (P3), as well as the passive margins of the continent in the southern and east-
 460 ern parts (P10). Regions with thicker crust (45–55 km) are observed underneath the Wyoming
 461 craton (tectonic province T2) and Trans-Hudson orogen (T3) as well as within the pre-
 462 cambrian building blocks towards the east (P6–P8; T4–T8) and south-west that extend
 463 into the Colorado plateau (P4).

464 6.3 Tectonic regionalization

465 In order to embed the results in a geological context, we first extracted radial pro-
 466 files of temperature, S-wave velocity, and shear attenuation on a $2.5^\circ \times 2.5^\circ$ -grid and
 467 grouped them individually via k-means clustering according to their similarity, i.e., by
 468 minimizing the L_2 -distance to the mean profile of the respective cluster (MacQueen, 1967).
 469 This approach allows for identification of tectonic regions without any a priori constraints
 470 (e.g., Houser et al., 2008; Lekić & Romanowicz, 2011; Lekić et al., 2012; Calò et al., 2016).
 471 Consistent results were found for three clusters that are shown in Figure 8. The radial
 472 profiles for each parameter show specific characteristics that determine the clustering:
 473 1) temperature and depth of the intersection point of conductive geotherm and mantle
 474 adiabat; 2) amplitude and depth extent of upper mantle low-velocity zone; and 3) thick-
 475 ness of high- Q_μ lid.

476 When the mean profile for each location is projected onto a map (see insets in Fig-
 477 ure 8), a well-known trend that follows the tectonic division of the North American con-
 478 tinent appears. In particular, we are able to distinguish the tectonically active west (en-
 479 compassing physiographic provinces P1–P5), which is characterised by being relatively
 480 hot, of slow shear-wave velocity, and highly dissipative (red dots), from the colder, faster,
 481 and less dissipative older eastern parts (blue dots) that include the cratonic core and the

Table 3. Summary of thermo-chemical characteristics and discontinuity structure of the main tectonic regions identified through cluster analysis in Figure 8A. Parameters are: crustal thickness (Z_c), potential temperature (T_{pot}), lithosphere thickness (Z_{lit}), basalt fraction (f), Mg# (molar Mg/(Mg+Fe)), and depth to 410 (Z_{410}) and 660 (Z_{660}). Values represent the mean and standard deviation based on the distributions shown in Figures 9C,E and 12B,D.

Parameter	Tectonic region		
	TAW (tectonically active West)	CTR (central transition regions)	COE (cratonic-orogenic East)
Z_c	40 ± 5 km	44 ± 5 km	44 ± 4 km
T_{pot}	1490 ± 27 °C	1429 ± 37 °C	1413 ± 27 °C
Z_{lit}	100 ± 23 km	146 ± 31 km	208 ± 33 km
f	$13 \pm 4.5\%$	$11 \pm 3.0\%$	$10 \pm 3.6\%$
Mg#	0.904 ± 0.003	0.906 ± 0.002	0.907 ± 0.003
Z_{410}	424 ± 7 km	417 ± 6 km	416 ± 6 km
Z_{660}	660 ± 2 km	659 ± 2 km	658 ± 2 km

482 Appalachian mountains, i.e., parts of provinces P6–P9 and T2–T8. The third cluster (green
483 dots) represents an intermediate group of profiles distributed over the central and east-
484 ern parts that are sandwiched between red and blue regions. While these features sug-
485 gest that tectonic regions are mainly controlled by the thermal structure of the conti-
486 nental lithosphere, a compositional signal is also present (section 6.6). For the remain-
487 der of the discussion, we will refer to the tectonic regions identified in Figure 8A as the
488 tectonically active West (TAW; red), the central transition regions (CTR; green), and
489 the cratonic-orogenic East (COE; blue). Smoothed outlines of these regions are indicated
490 in the maps and an overview of the values observed for the thermo-chemical parameters
491 is given in Table 3.

492 6.4 Mantle temperature

493 For ease of comparison with literature estimates, we rely on the concept of poten-
494 tial temperature, T_{pot} , which is the temperature of the adiabatic mantle when extended
495 to the Earth’s surface (McKenzie & Bickle, 1988). We compute T_{pot} by linear extrap-
496 olation of the adiabatic mantle geotherm: $T_{\text{pot}} = T_{\text{lit}} - \nabla T \cdot Z_{\text{lit}}$, where we have em-
497 ployed an adiabatic gradient $\nabla T = (T_{410} - T_{\text{lit}})/(Z_{410} - Z_{\text{lit}})$ with T_{410} and Z_{410} rep-
498 resenting temperature at and depth of the 410, respectively. Uncertainties on T_{pot} av-
499 erage 35 °C and 43 °C for Ps and Sp RFs, respectively (Figure 6C–D). Figure 9A dis-
500 plays the interpolated values of the mean value of T_{pot} . As in Figure 8A, we observe a
501 clear east-west trend from low to high potential temperatures, reaching values of 1430–
502 1520 °C in region TAW, 1360–1470 °C in CTR, and 1350–1450 °C in COE, respectively.
503 We find large positive thermal anomalies underneath the Cascade Range (P1), the Basin
504 and Range province (P3), and Yellowstone Hotspot. The same general east-west pattern
505 was also observed in the thermal anomaly maps obtained by Khan et al. (2011) from in-
506 version of surface wave phase velocities, although of lower resolution, by Maguire et al.
507 (2018) from stacking of Ps RFs, and S. M. Hansen et al. (2015) from analysis of surface
508 wave tomographic models. We should note that thermal anomalies constrained by Sp
509 RFs could be biased by the basalt-rich nature of the inverted compositions (see Figure 6H).

510 We estimate that in these regions “normal” basalt fractions would cool the mantle lo-
 511 cally by up to $\sim 30\text{--}50$ °C (cf. supplementary Figure S.16).

512 6.5 Lithospheric thickness and structure

513 A map of the thickness of the thermal lithosphere is shown in Figure 9B. We em-
 514 phasize that lithospheric thickness refers to the depth (defined by Z_{lit}) at which the con-
 515 ductive geotherm intercepts the mantle adiabat. There is no apparent discontinuity as-
 516 sociated herewith and hence no converted phase; yet, the long-period part of the Sp RFs
 517 (cf. supplementary Figure S.15) is affected. Note that uncertainties on thermal lithospheric
 518 thickness are generally much smaller for Sp (17 km) than for Ps RFs (32 km) (Figure 6E–
 519 F). This arises because lithospheric Sp RFs are not obscured by crustal reverberations,
 520 as is the case for Ps RFs. Consequently, Ps RFs only provide indirect insight into litho-
 521 spheric structure via the sensitivity of the P410s and P660s to mantle temperature, which
 522 is controlled by both Z_{lit} and T_{lit} . However, as S-to-p measurements are sparse, we in-
 523 clude the results from Ps RFs for interpolating Z_{lit} .

524 The thinnest lithosphere (79–141 km) is found in region TAW, as also observed in
 525 previous studies that considered Ps and/or Sp RFs (e.g., Li et al., 2007; Abt et al., 2010;
 526 Lekić et al., 2011; Levander & Miller, 2012; Hopper et al., 2014; S. M. Hansen et al., 2015).
 527 The exact shape of the thin-lithosphere branches that extend across the Rocky Moun-
 528 tains (P5) towards the Central plains (P6) are only constrained by few data points and
 529 hence are not interpreted further here. Region CTR shows an intermediate range in litho-
 530 spheric thickness of 85–187 km and coincides mostly with the western Great plains (P6),
 531 the New Madrid Seismic Zone (e.g., Zhang et al., 2009; C. Chen et al., 2014), and the
 532 mid-continental rift system (e.g., Stein et al., 2015). Finally, region COE is, as expected
 533 on account of its cratonic and orogenic nature, composed of relatively thick lithosphere
 534 (125–247 km). This negative correlation between potential temperature and lithospheric
 535 thickness observed in the maps is clearly visible in Figure 9C and is further illustrated
 536 in the tomographic cross sections shown in Figure 11, where lateral variations in thick-
 537 ness go hand-in-hand with variations in S-wave anomalies (see section 6.7) such that thick
 538 lithosphere is predominant in “cold” regions, whereas thin lithosphere is found in “hot-
 539 ter” regions.

540 We should note that some Sp RFs (e.g., 17-JCT, 32-SUSD, and 39-COWI) show
 541 complexities in the lithospheric part that are difficult to fit, which could potentially lead
 542 to a bias in thermal thickness estimates. These complexities have been attributed to mid-
 543 lithospheric discontinuities (MLDs) that were observed in Sp RFs from North America
 544 (e.g., Abt et al., 2010; Miller & Eaton, 2010; H. Yuan & Romanovicz, 2010; Lekić & Fis-
 545 cher, 2014; Kind et al., 2015; Calò et al., 2016) and elsewhere (e.g., Heit et al., 2007; Sav-
 546 age & Silver, 2008; L. Chen, 2009; Ford et al., 2010; Wölbern et al., 2012; Sodoudi et al.,
 547 2013). Processes capable of creating MLDs have been discussed extensively by Selway
 548 et al. (2015). In a recent study, Kind et al. (2020) has pointed out that MLDs could re-
 549 sult from the use of “inexact” filtering and deconvolution. Instead Kind et al. (2020) di-
 550 rectly summed waveforms to obtain RF stacks as a result of which MLDs, for example,
 551 were less apparent and point to the importance of careful data processing. While unob-
 552 jectionable, this is of less importance in this study, inasmuch as the problems that be-
 553 set imaging and interpretation are avoided in an inversion, where the same processing
 554 steps are applied to synthetic and observed data.

555 6.6 Mantle composition

556 Mantle composition (basalt fraction) primarily affects the sharpness of the 410 and
 557 660 seismic discontinuities through its influence on RF amplitudes rather than the tim-
 558 ing of converted waves (see supplementary Figure S.15). This is opposite to the effect
 559 of temperature, which primarily affects the depth of the 410 and 660 and, through that,
 560 travel time of the converted phases. This separation of sensitivity allows us to decou-

561 ple the parameters. Basalt fractions estimated from Ps RFs vary on average from 0 to
 562 25%, i.e., within the Harzburgite to Pyrolite range with uncertainties around 5% (cf. Fig-
 563 ure 6G). In comparison, Sp RF-estimated basalt fractions show larger uncertainties (9.5%;
 564 cf. Figure 6H) and appear to cluster toward the upper end of the prior ($f = 50\%$), in
 565 disagreement with the Ps RF-derived results and other studies (e.g., Khan et al., 2011;
 566 Maguire et al., 2018). The inferred basalt-enrichment is likely related to the reduced sen-
 567 sitivity of the S410p to composition, because of the generally small amplitudes of S410p
 568 relative to P410s. However, as noted earlier, this only has a small effect on thermal es-
 569 timates due to the first-order decoupling of temperature and composition. Consequently,
 570 we exclude Sp RF-derived information from the compositional map (Figure 9D).

571 For present purposes, we express composition by means of the Mg#, which is com-
 572 puted as $\text{Mg}/(\text{Mg}+\text{Fe})$ (molar) (cf. Table 1), where high/low Mg# is indicative of de-
 573pleted/fertile mantle, i.e., low/high basalt fraction, respectively. While most of the man-
 574 tle across the continent appears to be made up of relatively depleted compositions (Fig-
 575 ure 9D), region TAW is found to be slightly more fertile ($f = 13 \pm 4.5\%$, $\text{Mg\#} \sim 0.90$)
 576 in comparison to regions CTR and COE (COE: $f = 10 \pm 3.6\%$, $\text{Mg\#} \sim 0.91$), similar
 577 to the results of Khan et al. (2011). Local enrichment of basalt underneath the conti-
 578 nent could correspond to traces of active (Cascadia) and ancient subduction zones (Far-
 579 allon). The location of these anomalies are in agreement with the results by Maguire et
 580 al. (2018).

581 6.7 Shear-wave velocity structure

582 In the following, we focus on models of isotropic elastic S-wave velocity. Figure 10
 583 shows S-wave velocity images of the upper mantle and MTZ. For comparison, analogous
 584 plots for two tomographic models, US-SL-2014 (Schmandt & Lin, 2014) and SL2013NA
 585 (Schaeffer & Lebedev, 2014), are shown in the supplementary material (Figures S.22–
 586 S.25). To illustrate lateral variations in structure further, we also present cross sections
 587 (Figure 11) along three east-west and north-south profiles (magenta lines in Figure 2C).
 588 From these tomographic images, the following observations can be made:

589 1) S-wave velocity anomalies in the upper mantle (100–300 km) closely follow the
 590 tectonic regionalization and appear to be dominated by the lithospheric signature in that
 591 velocities are high/low in regions with a deep/shallow lithosphere, respectively. These
 592 observations are particularly apparent in the east-west trending cross sections, where the
 593 lithosphere slowly thickens and S-wave velocities decrease when passing from region TAW
 594 to CTR underneath the eastern Rocky Mountains flank (P5 to P6). The large variations
 595 in lithosphere thickness (70–250 km) affect the extent and amplitude of the upper man-
 596 tle low-velocity zone (Figure 8B), including large lateral velocity variations of $\pm 5.1\%$ at
 597 100 km depth. Amplitudes aside, similar observations were made in models SL2013NA
 598 and US-SL-2014 (supplementary Figures S.22–S.25) and other regional tomographic mod-
 599 els (e.g., Grand & Helmberger, 1984; van der Lee & Frederiksen, 2005; Nettles & Dziewon-
 600 ski, 2008; Bensen et al., 2009; H. Yuan & Romanovicz, 2010; Khan et al., 2011; H. Yuan
 601 et al., 2011, 2014; W. Shen & Ritzwoller, 2016; Krischer et al., 2018).

602 2) We are able to image mantle features underneath the western margin of the con-
 603 tinent (region TAW), where volcanism, accretion, and extensive tectonics are the likely
 604 surface expression of ancient and active subduction (e.g., Sonder & Jones, 1999; Dick-
 605 inson, 2004; Humphreys, 2009). We observe localized high-velocity anomalies in the north
 606 that move further inland and southward at greater depths (Figure 11B) and probably
 607 represent fragmented pieces of the Juan de Fuca, Gorda, and Farallon slabs (e.g., Sigloch,
 608 2011; Portner & Hayes, 2018). We further see a dominant low-velocity band parallel to
 609 the Pacific coast, which, at shallow depths, forms a circular structure around the Col-
 610 orado plateau (P4) that extends towards Yellowstone. Similar features were identified
 611 by Becker (2012) in a comparison of tomographic models of the region (Roth et al., 2008;
 612 Burdick et al., 2008, 2010; Obrebski et al., 2010, 2011; Schmandt & Humphreys, 2010,
 613 2011; James et al., 2011; Sigloch, 2011). However, it has to be pointed out that: 1) res-

614 olution of our model is low because of reduced data coverage at shallow depth at the flank
 615 of the eastern Rocky Mountains (P5); and 2) high basalt fractions, as inferred from Sp
 616 RFs, tend to decrease velocity within the MTZ, which exaggerates low-velocity anom-
 617 alies in regions where Ps RF data points are limited.

618 3) Considering the central and eastern part (regions CTR and COE), we find mul-
 619 tiple high-velocity anomalies that extend to the MTZ, where a roughly north-south aligned
 620 band underneath the Great plains (P6) is the most pronounced feature (see east-west
 621 cross section). These anomalies could be interpreted as remnant pieces of the Farallon
 622 or Laramide slabs, although differences in shape relative to other studies are apparent
 623 (e.g., Sigloch, 2011; Schmandt & Lin, 2014; Porritt et al., 2014).

624 4) Toward the bottom of the upper mantle, amplitudes of shear-wave anomalies
 625 generally decrease, but again increase significantly at and around 400 km depth as olivine
 626 transforms to wadsleyite. Lateral velocity variations are larger than those above and be-
 627 low the transition and emphasizes the importance of considering phase-induced varia-
 628 tions in addition to variations arising purely from volumetric velocity perturbations. Struc-
 629 ture in and around the MTZ is complex and shows significant topography, particularly
 630 on the 410 (Figure 12A). As shown in Figure 12B, we find that the 410 occurs deeper
 631 (409–432 km) in “hot” regions (TAW) than in “colder” parts (404–423 km in CTR; 401–
 632 422 km in COE). To compositionally achieve an equivalent 410-depth variation (>30 km),
 633 basalt fraction would have to change by >50% (see supplementary Figure S.16), which
 634 corresponds to more than the total compositional variation observed across the whole
 635 study area (Figure 9D). This suggests that composition is of secondary nature in deter-
 636 mining topography on the 410.

637 5) In contrast to the large peak-to-peak amplitudes of >30 km for the 410, lateral
 638 variations of the 660 are only ± 5 km (Figure 12C) and there appears to be little corre-
 639 lation with temperature (Figures 12D). Instead, the dependence of the 660 on temper-
 640 ature and composition is highly non-linear (Figure S.14) and also affected by the trans-
 641 formation of garnet, whose relative importance increases as temperature and basalt frac-
 642 tion increases (e.g., Weidner & Wang, 1998; Hirose, 2002; Xu et al., 2008; Khan et al.,
 643 2009) (see also supplementary Figures S.3 and S.4 of Munch et al. (2018)). Since the Clapey-
 644 ron slopes for the transformations of garnet and ringwoodite are opposite in sign (Hirose,
 645 2002; Liu et al., 2018), the garnet phase transition would follow the behaviour of the 410
 646 and move deeper in regions of elevated temperature.

647 6) As a result, MTZ-thickness (Figure 12E) is largely controlled by the topogra-
 648 phy on the 410 and is thinner in region TAW (~ 220 – 250 km) than in CTR and COE
 649 (~ 230 – 260 km). The 410 beneath the western USA (TAW), where two strong depres-
 650 sions separated by a high-elevation band across northern Nevada (see Figure 11B) are
 651 observable, agrees well with other Ps and Sp RF studies of the region (Cao & Lavender,
 652 2010; Tauzin et al., 2013; Gao & Liu, 2014) and possibly relates to subduction. In con-
 653 trast, the 660 and hence MTZ thickness varies more across the aforementioned studies.
 654 This first and foremost reflects the use of different imaging methods and different ref-
 655 erence models in order to convert receiver functions from time to depth. Furthermore,
 656 to the east of the Rocky Mountain front (CTR and COE), our inferred 410 and hence
 657 MTZ thickness tends to “normal” values, in overall agreement with the continental-scale
 658 MTZ model of Gao and Liu (2014). Further to this, Gao and Liu (2014) found, in agree-
 659 ment with Maguire et al. (2018), the MTZ to be locally thicker underneath the Great
 660 Plains (P6), which they attributed to remnants of the Farallon or Laramide slabs. Al-
 661 though less prominent, similar MTZ anomalies are also observed here.

662 7 Comparison of seismic and thermobarometric constraints

663 Assessment of the chemical and petrological characteristics of erupted lavas can pro-
 664 vide complementary information to seismic inversions to understand the thermo-chemical
 665 structure of the underlying mantle. In order to facilitate this comparison, we compiled
 666 whole rock chemical analyses of ~ 500 primitive basaltic rocks from the western USA,

667 filtered for basalts with eruption ages younger than 5 Ma and with MgO contents ≥ 8 wt%
 668 (see section S.7 for details). The composition of each sample was inverted in order to solve
 669 for the mean pressure and temperature of melt segregation according to the thermobarom-
 670 eter of Lee et al. (2009) to create an internally-consistent database. The resultant es-
 671 timates on (minimum) lithosphere thickness and mantle potential temperature for each
 672 sample have uncertainties of about 17 km and 50 °C, respectively. Our results are con-
 673 sistent with those of Plank and Forsyth (2016) to within (± 20 °C) and (± 15 km) for over-
 674 lapping localities.

675 Comparison between petrological and seismological T-P estimates is subject to caveats
 676 associated with i) the differing spatial coverage, and ii) the degree to which phase- and/or
 677 compositional changes influence the seismic inversion (section 4.1). To account for the
 678 locally-confined spatial sensitivity of thermobarometry relative to seismic wavelengths
 679 (cf. section 2.2.3), we masked cells beyond a radius of 1.5° to a sample location. Litho-
 680 spheric thickness is more difficult to compare given the reduced data coverage in the western-
 681 most USA and the imposed seismic lower bound of 70 km.

682 With these considerations in mind, the interpolated results from thermobarome-
 683 try are shown in Figure 13A–B, while the difference to seismically derived potential tem-
 684 perature estimates are presented in Figure 13C–D. The major magmatic provinces are
 685 demarcated on the basis of both seismic and petrological inversions (Figure 9 and 13).
 686 Thermally anomalous mantle is observed underneath the Cascade range (northern P1)
 687 and the Snake River Plain (eastern P2) towards Yellowstone Hotspot, and particularly
 688 under the Basin and Range province (P3) in southern Nevada, extending towards the
 689 southeast in the Rio Grande rift. Both methods agree on the relative amplitude of ther-
 690 mal anomalies, but differ in absolute values.

691 The largest temperature discrepancies, in which seismological estimates are 100–
 692 250 °C higher with respect to thermobarometric inversions (cf. Figure 13C–D), are pri-
 693 marily observed along the Cascade arc parallel to the Pacific coast (P1). The petrologically-
 694 derived potential temperatures, 1300–1350 °C, are in agreement with other thermobarom-
 695 etric estimates (Grove et al., 2002; Leeman et al., 2005), whereas temperatures derived
 696 from the seismic model may reflect the cumulative effects of increased H_2O , fO_2 , and
 697 melt fraction underneath this region, none of which are considered. Influx of water and
 698 oxidising melts from the downgoing slab into the mantle wedge are characteristics of sub-
 699 duction zones, with the net effect being that increasing Fe^{3+} in olivine results in increased
 700 dissipation of the shear modulus (Cline II et al., 2018), such that more oxidised/water-
 701 rich mantle appears seismically slower (and therefore hotter). Other regions show smaller
 702 differences (0–100 °C), and pertain to largely anhydrous tholeiitic provinces (Snake River
 703 Plain, Southern Nevada, and New Mexico) formed by decompression melting of upwelling
 704 asthenosphere (Fitton et al., 1991; Feuerbach et al., 1993; Leeman et al., 2009). This agree-
 705 ment therefore empirically verifies the accuracy of the seismic inversion in quantifying
 706 the thermo-chemical characteristics of more typical upper mantle.

707 The strength of this comparison lies in that surficial expressions of thermal anoma-
 708 lies may be linked to deep mantle structures. It also highlights the sensitivity of seismologically-
 709 derived temperature-depth estimates to the specific petrological characteristics of the man-
 710 tle, which changes with tectonic setting. Correctly accounting for these variations could
 711 help solve ambiguity in the chemical and isotopic signatures of eruptive provinces by imag-
 712 ing the thermal state of the underlying mantle in more detailed seismic and petrolog-
 713 ical surveys in future.

714 8 Summary and conclusions

715 In this paper, we proposed a methodology for processing, modeling, and inversion
 716 of multi-frequency P-to-s and S-to-p converted body waves (receiver functions) and ap-
 717 plied it to data recorded by USArray to perform a tomographic study of crust and man-
 718 tle beneath the North American continent.

Careful data selection and processing has been found to be a central step in the construction of Sp receiver functions, since these are typically prone to be noisy and sense distinct mantle regions depending on source-receiver configuration. To properly account for this, we binned data into different back-azimuth bins and considered these separately. To further increase the robustness of our Sp RF stacks, we augmented the latter by combining data from USArray reference and transportable stations. Ultimately, only high-quality Ps and Sp receiver functions with clear conversions at the Moho, lithosphere, 410, and 660 were retained for inversion. Finally, to ensure consistency between observed and synthetic RF waveform amplitudes, processing of modeled waveforms mimicked that applied to real data in detail. As part of waveform verification, we also conducted a validation of our approach to computing synthetic waveforms in 1-D models by comparing these to full waveform synthetics computed in a 3-D velocity model.

Relying on a thermodynamic formulation, the forward model consisted of first computing seismic velocity and density models via Gibbs' free energy-minimization, followed by seismic waveform modeling to construct maps of the crust and thermo-chemical mantle structure underneath the contiguous USA. We were able to identify three major tectonic regions based on similarities in radial temperature and S-wave velocity structure:

1) The tectonically active West (TAW), comprising regions west of the Rocky Mountains, is characterised compositionally as more fertile ($Mg\# \sim 0.90$), physically by a thinner lithosphere (100 ± 23 km), and thermally by higher mantle potential temperatures (1490 ± 27 °C). Consequently, shallow upper mantle S-wave velocity is strongly diminished (by up to -5%), shear-attenuation is increased, and the 410-km seismic discontinuity is shifted to greater depths (424 ± 7 km).

2) The cratonic-orogenic East (COE), including most of the continent to the east of the Great Plains, is compositionally more depleted ($Mg\# \sim 0.91$) and colder (1413 ± 27 °C), underlain by an overall thicker lithosphere (208 ± 33 km). Accordingly, S-wave velocity is higher (by up to $+5\%$), shear-attenuation is decreased, and the 410 appears at shallower depths (416 ± 6 km).

3) The Central transition regions (CTR) represent tectonic regions with intermediate properties in-between those of TAW and COE.

Despite being able to image well-known mantle features such as traces of active and ancient subduction or the Yellowstone plume, we note that resolving the exact shape and extent of such 3-D volumetric features by our method is limited by two factors: 1) we do not solve the inverse problem in a fully 3-D framework, but rather use a 1-D formulation to build a 3-D model a posteriori, and 2) converted waves are not directly sensitive to volumetric velocity changes, but rather to velocity contrasts across discontinuities. Further limitations of our method arise from the use of isentropes in modeling mantle thermal structure, end-member compositional model, and the assumption of an equilibrium assemblage configuration. Further, the absence of thermodynamic data, for now, involving melt-, and water-bearing systems might bias our results in certain regions, such as underneath the Cascades arc, as evidenced in the apparent mismatch with petrological estimates. Yet in spite of these limitations, a fully equilibrated, compositionally uniform, adiabatic, and dry mantle nevertheless provides an excellent fit to the observed seismic data. Our combination of geophysically-derived potential temperature- and lithospheric thickness estimates to those obtained from thermobarometric inversions of volcanic rock chemistry in the western USA show first-order agreement, permitting the assessment of broad-scale mantle melting conditions and their magmatic expression. This integrated approach represents a promising avenue for providing multidimensional insight into crustal tectonic structures and regimes and their link with deep mantle processes.

Acknowledgments

We thank the editor, M. Bostock for editorial handling, the associate editor V. Lekić, H. Yuan, and an anonymous reviewer for valuable comments that helped improve the quality of the manuscript. This study is supported by a grant from the Swiss Federal

773 Institute of Technology (ETH, project number 1-003490-000). B. T. has received fund-
 774 ing from the European Union’s Horizon 2020 research and innovation program under the
 775 Marie Skłodowska-Curie grant agreement No. 793824. P. A. S. acknowledges support from
 776 the Swiss National Science Foundation via an Ambizione Fellowship (No. 180025). F. D. M.
 777 is supported by the Swiss National Science Foundation (Project No. 159907 and 191892).
 778 The facilities of Incorporated Research Institutions for Seismology (IRIS) Data Services,
 779 and specifically the IRIS Data Management Center, were used for access to waveforms
 780 and related metadata. IRIS Data Services are funded through the Seismological Facil-
 781 ities for the Advancement of Geoscience (SAGE) Award of the National Science Founda-
 782 tion under Cooperative Support Agreement EAR-1851048. Data from the transportable
 783 array network were made freely available as part of the EarthScope USArray facility, op-
 784 erated by IRIS and supported by the National Science Foundation, under Cooperative
 785 Agreements EAR-1261681. Seismic data were downloaded via ObspyDMT (Hosseini &
 786 Sigloch, 2017) and processed using Obspy (Krischer et al., 2015) and the Python-package
 787 “rf” (Eulenfeld, 2020). Perple_X is available on www.perplex.ethz.ch and we use the
 788 CMAES-implementation by N. Hansen et al. (2019). Maps were created by means of the
 789 Basemap Matplotlib Toolkit (matplotlib.org/basemap/). Tomographic mantle mod-
 790 els SL2013NA, US-SL-2014, and GyPSuM were downloaded from IRIS-EMC ([ds.iris](http://ds.iris.edu/ds/products/emc/)
 791 [.edu/ds/products/emc/](http://ds.iris.edu/ds/products/emc/)), while model S362ANI and related codes are available on [www](http://www.ldeo.columbia.edu/~ekstrom/Projects/3D/BK/models.html)
 792 [.ldeo.columbia.edu/~ekstrom/Projects/3D/BK/models.html](http://www.ldeo.columbia.edu/~ekstrom/Projects/3D/BK/models.html). Computations were
 793 performed on the clusters Euler (ETH) and Piz Daint (CSCS). Computations on Piz Daint
 794 were supported by the Swiss National Supercomputing Centre (CSCS) under Project ID
 795 s922. We are grateful to M. Afanasiev, M. van Driel, S. Thrastarsson, L. Krischer, and
 796 W. Halter for support in simulating 3-D waveforms using the Salvus software package
 797 (www.mondaic.com).

798 References

- 799 Abt, D. L., Fischer, K. M., French, S. W., Ford, H. A., Yuan, H., & Romanowicz,
 800 B. (2010). North American lithospheric discontinuity structure imaged by
 801 Ps and Sp receiver functions. *J. Geophys. Res.*, *115*(B09301), 1-24. doi:
 802 10.1029/2009JB006914
- 803 Afanasiev, M., Boehm, C., vanDriel, M., Krischer, L., Rietmann, M., May, D. A.,
 804 ... Fichtner, A. (2019). Modular and flexible spectral-element waveform mod-
 805 elling in two and three dimensions. *Geophys. J. Int.*, *216*(3), 1675-1692. doi:
 806 10.1093/gji/ggy469
- 807 Afonso, J. C., Rawlinson, N., Yang, Y., Schutt, D. L., Jones, A. G., Fullea, J., &
 808 Griffin, W. L. (2016). 3D multiobservable probabilistic inversion for the com-
 809 positional and thermal structure of the lithosphere and upper mantle: III.
 810 Thermochemical tomography in the WesternCentral U.S. *J. Geophys. Res.*,
 811 *121*(B10), 7337-7370. doi: 10.1002/2016JB013049
- 812 Alibert, C., Michard, A., & Albarède, F. (1986). Isotope and trace element geochem-
 813 istry of Colorado Plateau volcanics. *Geochim. Cosmochim. Acta*, *50*(12), 2735-
 814 2750. doi: 10.1016/0016-7037(86)90223-1
- 815 Amante, C., & Eakins, B. W. (2009). Etopo1 1 arc-minute global relief model:
 816 Procedures, data sources and analysis. *NOAA Technical Memorandum*
 817 *NESDIS NGDC-24. National Geophysical Data Center, NOAA.* doi:
 818 10.7289/V5C8276M
- 819 Andrews, J., & Deuss, A. (2008). Detailed nature of the 660 km region of the man-
 820 tle from global receiver function data. *J. Geophys. Res.*, *113*(B06304). doi: 10
 821 .1029/2007JB005111
- 822 Arculus, R. J., & Gust, D. A. (1995). Regional Petrology of the San Francisco Vol-
 823 canic Field, Arizona, USA. *J. Petrol.*, *36*(3), 827-861. doi: 10.1093/petrology/
 824 36.3.827
- 825 Artemieva, I. M., & Mooney, W. D. (2001). Thermal thickness and evolution of Pre-

- 826 cambrian lithosphere: A global study. *J. Geophys. Res.*, *106*(B6), 16387-16414.
827 doi: 10.1029/2000JB900439
- 828 Bacon, C. R., Bruggman, P. E., Christiansen, R. L., Clynne, M. A., Donnelly-Nolan,
829 J. M., & Hildreth, W. (1997). Primitive magmas at five Cascade volcanic
830 fields: melts from hot, heterogeneous sub-arc mantle. *Can. Mineral.*, *35*(2),
831 397-423.
- 832 Bagheri, A., Khan, A., Al-Attar, D., Crawford, O., & Giardini, D. (2019). Tidal
833 response of Mars constrained from laboratory-based viscoelastic dissipa-
834 tion models and geophysical data. *J. Geophys. Res.: Planets*, *124*. doi:
835 10.1029/2019JE006015
- 836 Beard, B. L., & Glazner, A. F. (1998). Petrogenesis of isotopically unusual Pliocene
837 olivine leucitites from Deep Springs Valley, California. *Contrib. Mineral.
838 Petrol.*, *133*, 402-417. doi: 10.1007/s004100050462
- 839 Becker, T. W. (2012). On recent seismic tomography for the western United States.
840 *Geochem. Geophys. Geosyst.*, *13*(Q01W10). doi: 10.1029/2011GC003977
- 841 Bensen, G. D., Ritzwoller, M. H., & Yang, Y. (2009). A 3-D shear veloc-
842 ity model of the crust and uppermost mantle beneath the United States
843 from ambient seismic noise. *Geophys. J. Int.*, *177*, 1177-1196. doi:
844 10.1111/j.1365-246X.2009.04125.x
- 845 Bercovici, D., & Karato, S.-I. (2003). Whole-mantle convection and the transition-
846 zone water filter. *Nature*, *425*(6953), 39-44.
- 847 Bina, C. R., & Helffrich, G. (1994). Phase transition Clapeyron slopes and transition
848 zone seismic discontinuity topography. *J. Geophys. Res.*, *99*(B8), 15853-15860.
849 doi: 10.1029/94JB00462
- 850 Bock, G. (1994). Multiples as precursors to S, SKS and ScS. *Geophys. J. Int.*, *119*,
851 421-427.
- 852 Boyce, A., Bastow, I. D., Golos, E. M., Rondenay, S., Burdick, S., & van der Hilst,
853 R. (2019). Variable modification of continental lithosphere during the Protero-
854 zoic Grenville orogeny: Evidence from teleseismic P-wave tomography. *Earth
855 Planet. Sci. Lett.*, *525*(115763). doi: 10.1016/j.epsl.2019.115763
- 856 Browne, B., Bursik, M., Deming, J., Louros, M., Martos, A., & Stine, S. (2010).
857 Eruption chronology and petrologic reconstruction of the ca. 8500 yr
858 B.P. eruption of Red Cones, southern Inyo chain, California. *GSA Bulletin*,
859 *122*(9-10), 1401-1422. doi: 10.1130/B30070.1
- 860 Buehler, J. S., & Shearer, P. M. (2017). Uppermost mantle seismic velocity struc-
861 ture beneath USArray. *J. Geophys. Res. Solid Earth*, *122*, 436-448. doi: 10
862 .1002/2016JB013265
- 863 Burdick, S., Li, C., Martynov, V., Cox, T., Eakins, J., Mulder, T., ... van der Hilst,
864 R. D. (2008). Upper Mantle Heterogeneity beneath North America from Travel
865 Time Tomography with Global and USArray Transportable Array Data. *Seis-
866 mol. Res. Lett.*, *79*(3), 384-392. doi: 10.1785/gssrl.79.3.384
- 867 Burdick, S., van der Hilst, R. D., Vernon, F. L., Martynov, V., Cox, T., Eakins, J.,
868 ... Pavlis, G. L. (2010). Model Update January 2010: Upper Mantle Hetero-
869 geneity beneath North America from Traveltime Tomography with Global and
870 USArray Transportable Array Data. *Seismol. Res. Lett.*, *81*(5), 689-693. doi:
871 10.1785/gssrl.81.5.689
- 872 Calò, M., Bodin, T., & Romanowicz, B. (2016). Layered structure in the upper man-
873 tle across North America from joint inversion of long and short period seismic
874 data. *Earth Planet. Sci. Lett.*, *449*, 164-175. doi: 10.1016/j.epsl.2016.05.054
- 875 Cao, A., & Lavender, A. (2010). High-resolution transition zone structures of
876 the Goreda Slab beneath the western United States: Implication for deep-
877 water subduction. *J. Geophys. Res.*, *115*(B07301), 1-13. doi: 10.1029/
878 2009JB006876
- 879 Chen, C., Zhao, D., & Wu, S. (2014). Crust and upper mantle structure of the New
880 Madrid Seismic Zone: Insight into intraplate earthquakes. *Phys. Earth Planet.*

- 881 *Inter.*, 230, 1-14. doi: 10.1016/j.pepi.2014.01.016
- 882 Chen, C., Zhao, D., & Wu, S. (2015). Tomographic imaging of the Cascadia sub-
883 duction zone: Constraints on the Juan de Fuca slab. *Tectonophysics*, 648, 73-
884 88. doi: 10.1016/j.tecto.2015.02.012
- 885 Chen, L. (2009). Lithospheric structure variations between the eastern and central
886 North China Craton from S- and P-receiver function migration. *Phys. Earth
887 Planet. Inter.*, 173, 216-227. doi: 10.1016/j.pepi.2008.11.011
- 888 Clark, A. N., & Lesher, C. E. (2017). Elastic properties of silicate melts: Impli-
889 cations for low velocity zones at the lithosphere-asthenosphere boundary. *Sci.
890 Adv.*, 3(12), 1-5. doi: 10.1126/sciadv.1701312
- 891 Cline II, C. J., Faul, U. H., David, E. C., Berry, A. J., & Jackson, I. (2018). Redox-
892 influenced seismic properties of upper-mantle olivine. *Nature*, 555(7696), 355-
893 358. doi: 10.1038/nature25764
- 894 Cole, E. D. (1989). *Petrogenesis of late Cenozoic alkalic basalt near the eastern
895 boundary of the Basin and Range, upper Grand Wash trough* (Unpublished
896 master's thesis). Las Vegas, University of Nevada.
- 897 Connolly, J. A. D. (2009). The geodynamic equation of state: What and how.
898 *Geochem. Geophys. Geosyst.*, 10(10), 1-19. doi: 10.1029/2009GC002540
- 899 Connolly, J. A. D., & Khan, A. (2016). Uncertainty of mantle geophysical properties
900 computed from phase equilibrium models. *Geophys. Res. Lett.*, 43, 1-9. doi: 10
901 .1002/2016GL068239
- 902 Cottaar, S., & Deuss, A. (2016). Large-scale mantle discontinuity topography be-
903 neath Europe: Signature of akimotoite in subducting slabs. *J. Geophys. Res.:
904 Solid Earth*, 121(1), 279-292. doi: 10.1002/2015JB012452
- 905 Crotwell, H. P., Owens, T. J., & Ritsema, J. (1999). The TauP Toolkit: Flexible
906 seismic travel-time and ray-path utilities. *Seismol. Res. Lett.*, 70, 154-160. doi:
907 10.1785/gssrl.70.2.154
- 908 Dickinson, W. R. (2004). Evolution of the North American Cordillera. *Annu. Rev.
909 Earth Planet. Sci.*, 32, 13-45. doi: 10.1146/annurev.earth.32.101802.120257
- 910 Dueker, K. G., & Sheehan, A. F. (1997). Mantle discontinuity structure from mid-
911 point stacks of converted P to S waves across the Yellowstone hotspot track. *J.
912 Geophys. Res.*, 102(B4), 8313-8327. doi: 10.1029/96JB03857
- 913 Dungan, M. A., Lindstrom, M. M., McMillan, N. J., Moor bath, S., Hoefs, J.,
914 & Haskin, L. A. (1986). Open system magmatic evolution of the Taos
915 Plateau volcanic field, northern New Mexico: 1. The petrology and geochem-
916 istry of the Servilleta Basalt. *J. Geophys. Res.*, 91(B6), 5999-6028. doi:
917 10.1029/JB091iB06p05999
- 918 Dziewonski, A. M., & Anderson, D. L. (1981). Preliminary reference Earth model.
919 *Phys. Earth Planet. Inter.*, 25, 297-356. doi: 10.1016/0031-9201(81)90046-7
- 920 Dziewonski, A. M., Chou, T.-A., & Woodhouse, J. H. (1981). Determina-
921 tion of earthquake source parameters from waveform data for studies of
922 global and regional seismicity. *J. Geophys. Res.*, 86(B4), 2825-2852. doi:
923 10.1029/JB086iB04p02825
- 924 Earle, P. S., & Shearer, P. M. (1994). Characterization of Global Seismograms Us-
925 ing an Automatic-Picking Algorithm. *Bull. Seismol. Soc. Am.*, 84(2), 366-376.
- 926 Eaton, D. W., Darbyshire, F., Evans, R. L., Grütter, H., Jones, A. G., & Yuan,
927 X. (2009). The elusive lithosphere-asthenosphere boundary (LAB) beneath
928 cratons. *Lithos*, 109(1-2), 1-22. doi: 10.1016/j.lithos.2008.05.009
- 929 Efron, B., & Tibshirani, R. (1991). Statistical data analysis in the computer age.
930 *Science*, 253(5018), 390-395. doi: 10.1126/science.253.5018.390
- 931 Eilon, Z., Fischer, K. M., & Dalton, C. A. (2018). An adaptive Bayesian inversion
932 for upper-mantle structure using surface waves and scattered body waves. *Geo-
933 physics. J. Int.*, 214, 232-253. doi: 10.1093/gji/ggy137
- 934 Ekström, G., Nettles, M., & Dziewonski, A. M. (2012). The global CMT project
935 2004-2010: Centroid-moment tensors for 13,017 earthquakes. *Phys. Earth*

- 936 *Planet. Inter.*, 200-201, 1-9. doi: 10.1016/j.pepi.2012.04.002
- 937 Eulenfeld, T. (2020). rf: Receiver function calculation in seismology. *J. Open Source*
938 *Softw.*, 5(48), 1808. doi: 10.21105/joss.01808
- 939 Farmer, G. L., Glazner, A. F., Wilshire, H. G., Wooden, J. L., Pickthorn, W. J.,
940 & Katz, M. (1995). Origin of late Cenozoic basalts at the Cima volcanic
941 field, Mojave Desert, California. *J. Geophys. Res.*, 100(B5), 8399-8415. doi:
942 10.1029/95JB00070
- 943 Farra, V., & Vinnik, L. (2000). Upper mantle stratification by P and S receiver func-
944 tions. *Geophys. J. Int.*, 141(3), 699-712. doi: 10.1046/j.1365-246x.2000.00118
945 .x
- 946 Feldstein, S. N., & Lange, R. A. (1999). Pliocene Potassic Magmas from the Kings
947 River Region, Sierra Nevada, California: Evidence for Melting of a Subduction-
948 Modified Mantle. *J. Petrol.*, 40(8), 1301-1320. doi: 10.1093/etroj/40.8.1301
- 949 Fenneman, N. M. (1928). Physiographic divisions of the United States. *Ann. Assoc.*
950 *Am. Geogr.*, 18(4), 261-353.
- 951 Férot, A., & Bolfan-Casanova, N. (2012). Water storage capacity in olivine and
952 pyroxene to 14 GPa: Implications for the water content of the Earth's upper
953 mantle and nature of seismic discontinuities. *Earth Planet. Sci. Lett.*, 349-350,
954 218-230. doi: 10.1016/j.epsl.2012.06.022
- 955 Feuerbach, D. L., Smith, E., Walker, J. D., & Tangeman, J. A. (1993). The role
956 of the mantle during crustal extension: Constraints from geochemistry of
957 volcanic rocks in the Lake Mead area, Nevada and Arizona. *Geol. Soc.*
958 *Am. Bull.*, 105(12), 1561-1575. doi: 10.1130/0016-7606(1993)105<1561:
959 TROTMD>2.3.CO;2
- 960 Fitton, J. G., James, D., & Leeman, W. P. (1991). Basic Magmatism Associated
961 With Late Cenozoic Extension in the Compositional Variations in Space and
962 Time. *J. Geophys. Res.*, 96(B8), 13693-13711. doi: 10.1029/91JB00372
- 963 Flanagan, M. P., & Shearer, P. M. (1998). Global mapping of topography on tran-
964 sition zone velocity discontinuities by stacking SS precursors. *J. Geophys. Res.*,
965 103(B2), 2673-2692. doi: 10.1029/97JB03212
- 966 Ford, H. A., Fischer, K. M., Abt, D. L., Rychert, C. A., & Elkins-Tanton, L. T.
967 (2010). The lithosphereasthenosphere boundary and cratonic lithospheric
968 layering beneath Australia from Sp wave imaging. *Earth Planet. Sci. Lett.*,
969 300(3), 299-310. doi: 10.1016/j.epsl.2010.10.007
- 970 Freitas, D., Mathilake, G., Schiavi, F., Chantel, J., Bolfan-Casanova, N., Bouhifd,
971 M. A., & Andraut, D. (2017). Experimental evidence supporting a global melt
972 layer at the base of the Earth's upper mantle. *Nat. Commun.*, 8(2186). doi:
973 10.1038/s41467-017-02275-9
- 974 Fuchs, K., & Müller, G. (1971). Computation of synthetic seismograms with the
975 reflectivity method and comparison with observations. *Geophys. J. Int.*, 23(4),
976 417-433. doi: 10.1111/j.1365-246X.1971.tb01834.x
- 977 Gao, S. S., & Liu, K. H. (2014). Mantle transition zone discontinuities beneath the
978 contiguous United States. *J. Geophys. Res.: Solid Earth*, 119, 6452-6468. doi:
979 10.1002/2014JB011253
- 980 Geissler, W. H., Sodoudi, F., & Kind, R. (2010). Thickness of the central and east-
981 ern European lithosphere as seen by S receiver functions. *Geophys. J. Int.*,
982 181(2), 604-634. doi: 10.1111/j.1365-246X.2010.04548.x
- 983 Glazner, A. F., Lang Farmer, G., Hughes, W. T., Wooden, J. L., & Pickthorn, W.
984 (1991). Contamination of basaltic magma by mafic crust at Amboy and Pisgah
985 Craters, Mojave Desert, California. *J. Geophys. Res.*, 96(B8), 13673-13691.
986 doi: 10.1029/91JB00175
- 987 Grand, S. P., & Helmberger, D. V. (1984). Upper mantle shear structure of North
988 America. *Geophys. J. Int.*, 76(2), 399-438. doi: 10.1111/j.1365-246X.1984
989 .tb05053.x
- 990 Green, D. H., Hibberson, W. O., Kovács, I., & Rosenthal, A. (2010). Water and its

- influence on the lithosphereasthenosphere boundary. *Nature*, *467*, 448-451. doi: 10.1038/nature09369
- Green, N. L., & Sinha, A. K. (2005). Consequences of varied slab age and thermal structure on enrichment processes in the sub-arc mantle of the northern Cascadia subduction system. *J. Volcanol. Geotherm. Res.*, *140*(1-3), 107-132. doi: 10.1016/j.jvolgeores.2004.07.017
- Grove, T. L., Parman, S. W., Bowring, S. A., Price, R. C., & Baker, M. B. (2002). The role of an H₂O-rich fluid component in the generation of primitive basaltic andesites and andesites from the Mt. Shasta region, N California. *Contrib. Mineral. Petrol.*, *142*, 375-396. doi: 10.1007/s004100100299
- Hammersley, L., & De Paolo, D. J. (2006). Isotopic and geophysical constraints on the structure and evolution of the Clear Lake volcanic system. *J. Volcanol. Geotherm. Res.*, *153*, 331-356. doi: 10.1016/j.jvolgeores.2005.12.003
- Hansen, N., Akimoto, Y., & Baudis, P. (2019). *CMA-ES/pycma on Github*. Zenodo, DOI:10.5281/zenodo.2559634. doi: 10.5281/zenodo.2559634
- Hansen, N., & Ostermeier, A. (2001). Completely derandomized self-adaptation in evolution strategies. *Evol. Comput.*, *9*(2), 159-195. doi: 10.1162/106365601750190398
- Hansen, S. M., Dueker, K., & Schmandt, B. (2015). Thermal classification of lithospheric discontinuities beneath USArray. *Earth Planet. Sci. Lett.*, *431*, 36-47. doi: 10.1016/j.epsl.2015.09.009
- Hastings, W. K. (1970). Monte Carlo sampling methods using Markov chains and their applications. *Biometrika*, *57*(1), 97-109. doi: 10.2307/2334940
- Heit, B., Sodoudi, F., Yuan, X., Bianchi, M., & Kind, R. (2007). An S receiver function analysis of the lithospheric structure in South America. *Geophys. Res. Lett.*, *34*(L14307). doi: 10.1029/2007GL030317
- Helffrich, G. (2000). Topography of the Transition Zone Discontinuities. *Rev. Geophys.*, *38*(1), 141-158. doi: 10.1029/1999RG000060
- Helffrich, G. R., & Wood, B. J. (2001). The Earth's mantle. *Nature*, *412*(6613), 219-229. doi: 10.1038/35087500
- Hill, R. (1952). The elastic behaviour of a crystalline aggregate. *Proc. Phys. Soc. A*, *65*, 349-354. doi: 10.1088/03701298/65/5/307
- Hirose, K. (2002). Phase transitions in pyrolitic mantle around 670-km depth: implications for upwelling of plumes from the lower mantle. *J. Geophys. Res.*, *107*(B4). doi: 10.1029/2001JB000597
- Hirschmann, M. M. (2006). Water, Melting, and the Deep Earth H₂O Cycle. *Annu. Rev. Earth Planet. Sci.*, *34*, 629-653. doi: 10.1146/annurev.earth.34.031405.125211
- Hoffer, J. M. (1988). Late Cenozoic basalts of southwestern New Mexico. In G. H. Mack, T. F. Lawton, & S. G. Lucas (Eds.), *Cretaceous and Laramide Tectonic Evolution of Southwestern New Mexico* (p. 119-122). New Mexico Geological Society 39th Annual Fall Field Conference Guidebook.
- Hoffman, P. F. (1988). United plates of America, the birth of a craton: Early Proterozoic assembly and growth of Laurentia. *Annu. Rev. Earth Planet. Sci.*, *16*, 543-603. doi: 10.1146/annurev.earth.16.050188.002551
- Hoffman, P. F. (1989). Precambrian geology and tectonic history of North America. In A. W. Bally & A. R. Palmer (Eds.), *The Geology of North America - An Overview, vol. A*. Boulder, CO: The Geological Society of America.
- Hopper, E., Ford, H. A., Fischer, K. M., Lekić, V., & Fouch, M. J. (2014). The lithosphereasthenosphere boundary and the tectonic and magmatic history of the northwestern United States. *Earth Planet. Sci. Lett.*, *402*, 69-81. doi: 10.1016/j.epsl.2013.12.016
- Hosseini, K., & Sigloch, K. (2017). ObspyDMT: a Python toolbox for retrieving and processing large seismological data sets. *Solid Earth*, *8*, 1047-1070. doi: 10.5194/se-8-1047-2017

- 1046 Houser, C., Masters, G., Shearer, P., & Laske, G. (2008). Shear and compressional
 1047 velocity models of the mantle from cluster analysis of long-period waveforms.
 1048 *Geophys. J. Int.*, *174*, 195-212. doi: 10.1111/j.1365-246X.2008.03763.x
- 1049 Humphreys, E. (2009). Relation of flat subduction to magmatism and deformation
 1050 in the western United States. In *Backbone of the Americas: Shallow Sub-*
 1051 *duction, Plateau Uplift, and Ridge and Terrane Collision*. Geological Society of
 1052 America. doi: 10.1130/2009.1204(04)
- 1053 Jackson, I., & Faul, U. H. (2010). Grainsize-sensitive viscoelastic relaxation in
 1054 olivine: towards a robust laboratory-based model for seismological application.
 1055 *Phys. Earth Planet. Inter.*, *183*(1-2), 151-163. doi: 10.1016/j.pepi.2010.09.005
- 1056 James, D. E., Fouch, M. J., Carlson, R. W., & Roth, J. B. (2011). Slab fragmenta-
 1057 tion, edge flow and the origin of the Yellowstone hotspot track. *Earth Planet.*
 1058 *Sci. Lett.*, *311*(1-2), 124-135. doi: 10.1016/j.epsl.2011.09.007
- 1059 Jaupart, C., & Mareschal, J.-C. (1999). Thermal structure and thickness of conti-
 1060 nental roots. *Lithos*, *48*, 93-114. doi: 10.1016/S0419-0254(99)80007-X
- 1061 Karato, S., Ologboji, T., & Park, J. (2015). Mechanisms and geologic significance
 1062 of the mid-lithosphere discontinuity in the continents. *Nat. Geosci.*, *8*, 509-514.
 1063 doi: 10.1038/NGEO2462
- 1064 Karato, S., & Park, J. (2019). On the Origin of the Upper Mantle Seismic Discon-
 1065 tinuities. In H. Yuan & B. Romanowicz (Eds.), *Lithospheric Discontinuities*.
 1066 Washington, DC: American Geophysical Union. doi: 10.1002/9781119249740
 1067 .ch1
- 1068 Kawakatsu, H., Kumar, P., Takei, Y., Shinohara, M., Kanazawa, T., Araki,
 1069 E., & Suyehiro, K. (2009). Seismic Evidence for Sharp Lithosphere-
 1070 Asthenosphere Boundaries of Oceanic Plates. *Science*, *324*(5926), 499-502.
 1071 doi: 10.1126/science.1169499
- 1072 Kempton, P. D., Dungan, M. A., & Blanchard, D. P. (1987). Petrology and geo-
 1073 chemistry of xenolith-bearing alkalic basalts from the Geronimo Volcanic Field,
 1074 southeast Arizona; Evidence for polybaric fractionation and implications for
 1075 mantle heterogeneity. In *Mantle Metasomatism and Alkaline Magmatism*.
 1076 Geological Society of America. doi: 10.1130/SPE215-p347
- 1077 Kennett, B. L. N., & Engdahl, E. R. (1991). Traveltimes for global earthquake lo-
 1078 cation and phase identification. *Geophys. J. Int.*, *105*, 429-465. doi: 10.1111/
 1079 j.1365-246X.1991.tb06724.x
- 1080 Khan, A., Boschi, L., & Connolly, J. A. D. (2009). On mantle chemical and thermal
 1081 heterogeneities and anisotropy as mapped by inversion of global surface wave
 1082 data. *J. Geophys. Res.*, *114*(B09305), 1-21. doi: 10.1029/2009JB006399
- 1083 Khan, A., & Shankland, T. J. (2012). A geophysical perspective on mantle wa-
 1084 ter content and melting: Inverting electromagnetic sounding data using
 1085 laboratory-based electrical conductivity profiles. *Earth Planet. Sci. Lett.*,
 1086 *317-318*, 27-43. doi: 10.1016/j.epsl.2011.11.031
- 1087 Khan, A., Zunino, A., & Deschamps, F. (2011). The thermochemical and physi-
 1088 cal structure beneath the North American continent from Bayesian inversion
 1089 of surfacewave phase velocities. *J. Geophys. Res.*, *116*(B09304), 1-23. doi:
 1090 10.1029/2011JB008380
- 1091 Kind, R., Mooney, W. D., & Yuan, X. (2020). New insights into the struc-
 1092 tural elements of the upper mantle beneath the contiguous United States
 1093 from S-to-P converted seismic waves. *Geophys. J. Int.*, *222*, 646-659. doi:
 1094 10.1093/gji/ggaa203
- 1095 Kind, R., Yuan, X., & Kumar, P. (2012). Seismic receiver functions and the litho-
 1096 sphereasthenosphere boundary. *Tectonophysics*, *536-537*, 25-43. doi: 10.1016/
 1097 j.tecto.2012.03.005
- 1098 Kind, R., Yuan, X., Mechie, J., & Sodoudi, F. (2015). Structure of the upper man-
 1099 tle in the north-western and central United States from USArray S-receiver
 1100 functions. *Solid Earth*, *6*, 957970. doi: 10.5194/se-6-957-2015

- 1101 Knapmeyer-Endrun, B., Krüger, F., Geissler, W. H., & PASSEQ Working Group.
 1102 (2017). Upper mantle structure across the Trans-European Suture Zone im-
 1103 aged by S-receiver functions. *Earth Planet. Sci. Lett.*, *458*, 429-441. doi:
 1104 10.1016/j.epsl.2016.11.011
- 1105 Kohlstedt, D., Keppler, H., & Rubie, D. (1996). Solubility of water in the α , β and
 1106 γ phases of $(\text{Mg,Fe})_2\text{SiO}_4$. *Contrib. Mineral. Petrol.*, *123*(345357). doi: 10
 1107 .1007/s004100050161
- 1108 Kosarev, G., Kind, R., Sobolev, S. V., Yuan, X., Hanka, W., & Oreshin, S. (1999).
 1109 Seismic Evidence for a Detached Indian Lithospheric Mantle Beneath Tibet.
 1110 *Science*, *283*(5406), 1306-1309. doi: 10.1126/science.283.5406.1306
- 1111 Krischer, L., Fichtner, A., Boehm, C., & Igel, H. (2018). Automated Large-Scale
 1112 Full Seismic Waveform Inversion for North America and the North Atlantic. *J.*
 1113 *Geophys. Res.: Solid Earth*, *123*, 5902-5928. doi: 10.1029/2017JB015289
- 1114 Krischer, L., Megies, T., Barsch, R., Beyreuther, M., Lecocq, T., Caudron, C., &
 1115 Wassermann, J. (2015). ObsPy: a bridge for seismology into the scientific
 1116 Python ecosystem. *Comput. Sci. Discov.*, *8*(1). doi: 10.1088/1749-4699/8/1/
 1117 014003
- 1118 Kumar, P., Yuan, X., Kind, R., & Kosarev, G. (2005). The lithosphere-
 1119 asthenosphere boundary in the Tien Shan-Karakoram region from S re-
 1120 ceiver functions: Evidence for continental subduction. *Geophys. Res. Lett.*,
 1121 *32*(L07305), 1-4. doi: 10.1029/2004GL022291
- 1122 Kustowski, B., Ekström, G., & Dziewonski, A. M. (2008). Anisotropic shear-wave
 1123 velocity structure of the Earth's mantle: A global model. *J. Geophys. Res.*,
 1124 *113*(B06306). doi: 10.1029/2007JB005169
- 1125 Langmuir, C. H., Klein, E. M., & Plank, T. (1992). Petrological Systematics of Mid-
 1126 Ocean Ridge Basalts: Constraints on Melt Generation Beneath Ocean Ridges.
 1127 In *Mantle Flow and Melt Generation at MidOcean Ridges* (p. 183-280). Ameri-
 1128 can Geophysical Union (AGU). doi: 10.1029/GM071p0183
- 1129 Langston, C. A. (1979). Structure Under Mount Rainier, Washington, Inferred From
 1130 Teleseismic Body Waves. *J. Geophys. Res.*, *84*(B9), 4749-4762. doi: 10.1029/
 1131 JB084iB09p04749
- 1132 Laske, G., Masters, G., Ma, Z., & Pasyanos, M. (2013). Update on CRUST1.0 - A 1-
 1133 degree Global Model of Earth's Crust. In *Geophys. Res. Abstracts*, *15*, Abstract
 1134 EGU2013-2658.
- 1135 Lau, H., & Faul, U. (2019). Anelasticity from seismic to tidal timescales: Theory
 1136 and observations. *Earth Planet. Sci. Lett.*, *508*, 18-29. doi: 10.1016/j.epsl.2018
 1137 .12.009
- 1138 Lawrence, J. F., & Shearer, P. M. (2006). A global study of transition zone thick-
 1139 ness using receiver functions. *J. Geophys. Res.*, *111*(B06307), 1-10. doi: 10
 1140 .1029/2005JB003973
- 1141 Lee, C.-T. A., Luffi, P., Plank, T., Dalton, H., & Leeman, W. P. (2009). Constraints
 1142 on the depths and temperatures of basaltic magma generation on Earth and
 1143 other terrestrial planets using new thermobarometers for mafic magmas. *Earth*
 1144 *Planet. Sci. Lett.*, *279*(1-2), 20-33. doi: 10.1016/j.epsl.2008.12.020
- 1145 Leeman, W. P., Lewis, J. F., Everts, R. C., Conrey, R. M., & Streck, M. J. (2005).
 1146 Petrologic constraints on the thermal structure of the Cascades arc. *J. Vol-
 1147 canol. Geotherm. Res.*, *140*(1-3), 67-105. doi: 10.1016/j.jvolgeores.2004.07.016
- 1148 Leeman, W. P., Schutt, D. L., & Hughes, S. S. (2009). Thermal structure beneath
 1149 the Snake River Plain: Implications for the Yellowstone hotspot. *J. Volcanol.*
 1150 *Geotherm. Res.*, *188*(1-3), 5767. doi: 10.1016/j.jvolgeores.2009.01.034
- 1151 Lekić, V., Cottaar, S., Dziewonski, A., & Romanowicz, B. (2012). Cluster analysis
 1152 of global lower mantle tomography: A new class of structure and implications
 1153 for chemical heterogeneity. *Earth Planet. Sci. Lett.*, *357-358*, 68-77. doi:
 1154 10.1016/j.epsl.2012.09.014
- 1155 Lekić, V., & Fischer, K. M. (2014). Contrasting lithospheric signatures across the

- western United States revealed by Sp receiver functions. *Earth Planet. Sci. Lett.*, *402*, 90-98. doi: 10.1016/j.epsl.2013.11.026
- Lekić, V., & Fischer, K. M. (2017). Interpreting spatially stacked Sp receiver functions. *Geophys. J. Int.*, *210*(2), 874-886. doi: 10.1093/gji/ggx206
- Lekić, V., French, S. W., & Fischer, K. M. (2011). Lithospheric Thinning Beneath Rifted Regions of Southern California. *Science*, *334*, 783-787. doi: 10.1126/science.1208898
- Lekić, V., & Romanowicz, B. (2011). Tectonic regionalization without a priori information: A cluster analysis of upper mantle tomography. *Earth Planet. Sci. Lett.*, *308*, 151-160. doi: 10.1016/j.epsl.2011.05.050
- Levander, A., & Miller, M. S. (2012). Evolutionary aspects of lithosphere discontinuity structure in the western U.S. *Geochem. Geophys. Geosyst.*, *13*(7), 1-22. doi: 10.1029/2012GC004056
- Li, X., Yuan, X., & Kind, R. (2007). The lithosphereasthenosphere boundary beneath the western United States. *Geophys. J. Int.*, *170*, 700-710. doi: 10.1111/j.1365-246X.2007.03428.x
- Ligorria, J. P., & Ammon, C. J. (1999). Iterative Deconvolution and Receiver-Function Estimation. *Bull. Seismol. Soc. Am.*, *89*(5), 1395-1400.
- Liu, H., Wang, W., Jia, X., Leng, W., Zhongqing, W., & Sun, D. (2018). The combined effects of post-spinel and post-garnet phase transitions on mantle plume dynamics. *Earth Planet. Sci. Lett.*, *496*, 80-88. doi: 10.1016/j.epsl.2018.05.031
- Liu, K. H. (2003). Effects of inelasticity on the apparent depth and detectability of seismic discontinuities in the mantle. *Geophys. Res. Lett.*, *30*(9), 1455. doi: 10.1029/2002GL015264
- Lowry, A. R., & Pérez-Gussinyé, M. (2011). The role of crustal quartz in controlling Cordilleran deformation. *Nature*, *471*, 353-357. doi: 10.1038/nature09912
- Ma, X., & Lowry, A. R. (2017). USArray Imaging of Continental Crust in the Conterminous United States. *Tectonics*, *36*, 2882-2902. doi: 10.1002/2017TC004540
- MacQueen, J. B. (1967). Some Methods for classification and Analysis of Multivariate Observations. In *Proceedings of 5th Berkeley Symposium on Mathematical Statistics and Probability. Band 1* (p. 281-297). University of California Press.
- Maguire, R., Ritsema, J., & Goes, S. (2018). Evidence of Subduction-Related Thermal and Compositional Heterogeneity Below the United States From Transition Zone Receiver Functions. *Geophys. Res. Lett.*, *45*, 8913-8922. doi: 10.1029/2018GL078378
- Makushkina, A., Tauzin, B., Tkalčić, H., & Thybo, H. (2019). The Mantle Transition Zone in Fennoscandia: Enigmatic High Topography Without Deep Mantle Thermal Anomaly. *Geophys. Res. Lett.*, *46*, 1-11. doi: 10.1029/2018GL081742
- McKenzie, D., & Bickle, M. (1988). The volume and composition of melt generated by extension of the lithosphere. *J. Petrol.*, *29*(3), 625-679. doi: 10.1093/petrology/29.3.625
- Metropolis, N., Rosenbluth, A. W., Rosenbluth, M. N., Teller, A. H., & Teller, E. (1953). Equation of state calculations by fast computing machines. *J. Chem. Phys.*, *21*(6), 1087-1092. doi: 10.1063/1.1699114
- Miller, M. S., & Eaton, D. W. (2010). Formation of cratonic mantle keels by arc accretion: Evidence from S receiver functions. *Geophys. Res. Lett.*, *37*(L18305), 1-5. doi: 10.1029/2010GL044366
- Monna, S., Montuori, C., Piromallo, C., & Vinnik, L. (2019). Mantle Structure in the Central Mediterranean Region From P and S Receiver Functions. *Geochem. Geophys. Geosyst.*, *20*. doi: 10.1029/2019GC008496
- Mooney, W. D., & Kaban, M. K. (2010). The North American upper mantle: Density, composition, and evolution. *J. Geophys. Res.*, *115*(B12424), 1-24. doi: 10

- 1211 .1029/2010JB000866
- 1212 Mordick, B. E., & Glazner, A. (2006). Clinopyroxene thermobarometry of basalts
1213 from the Coso and Big Pine volcanic fields, California. *Contrib. Mineral.*
1214 *Petrol.*, *152*(1), 111-124. doi: 10.1007/s00410-006-0097-0
- 1215 Mosegaard, K., & Tarantola, A. (1995). Monte Carlo sampling of solutions to inverse
1216 problems. *J. Geophys. Res.*, *100*(B7), 12431-12447. doi: 10.1029/94JB03097
- 1217 Mosegaard, K., & Tarantola, A. (2002). Probabilistic Approach to Inverse Prob-
1218 lems. In *International handbook of earthquake and engineering seismology*
1219 (p. 237-265). Academic Press.
- 1220 Müller, G. (1985). The reflectivity method: a tutorial. *J. Geophys.*, *58*, 153-174.
- 1221 Munch, F. D., Khan, A., Tauzin, B., van Driel, M., & Giardini, D. (2020). Seis-
1222 mological evidence for thermo-chemical heterogeneity in Earth's continental
1223 mantle. *Earth Planet. Sci. Lett.*, *539*, 1-9. doi: 10.1016/j.epsl.2020.116240
- 1224 Munch, F. D., Khan, A., Tauzin, B., Zunino, A., & Giardini, D. (2018). Stochas-
1225 tic inversion of PtoS converted waves for mantle thermal and compositional
1226 structure: methodology and application. *J. Geophys. Res.: Solid Earth*, *123*,
1227 10706-10726. doi: 10.1029/2018JB016032
- 1228 Nakata, J. K. (1980). Distribution and petrology of the Anderson-Coyote Reservoir
1229 volcanic rocks, California. *U.S. Geological Survey Open-File Report*, *80-1256*.
- 1230 Nelson, P. L., & Grand, S. P. (2018). Lower-mantle plume beneath the Yellowstone
1231 hotspot revealed by core waves. *Nat. Geosci.*, *11*, 280-284. doi: 10.1038/s41561
1232 -018-0075-y
- 1233 Nettles, M., & Dziewonski, A. (2008). Radially anisotropic shear velocity structure
1234 of the upper mantle globally and beneath North America. *J. Geophys. Res.*,
1235 *113*(B02303). doi: 10.1029/2006JB004819
- 1236 Obrebski, M., Allen, R. M., Pollitz, F., & Hung, S.-H. (2011). Lithosphere-
1237 asthenosphere interaction beneath the western United States from the joint
1238 inversion of body-wave travel- times and surface-wave phase velocities. *Geo-*
1239 *phys. J. Int.*, *185*(2), 1003-1021. doi: 10.1111/j.1365-246X.2011.04990.x
- 1240 Obrebski, M., Allen, R. M., Xue, M., & Hung, S.-H. (2010). Slab-plume interaction
1241 beneath the Pacific Northwest. *Geophys. Res. Lett.*, *37*(L14305). doi: 10.1029/
1242 2010GL043489
- 1243 Peters, T. J., Menzies, M., Thirlwall, M., & Kyle, P. R. (2008). ZuniBandera vol-
1244 canism, Rio Grande, USA - Melt formation in garnet- and spinel-facies mantle
1245 straddling the asthenosphere-lithosphere boundary. *Lithos*, *102*(1-2), 295-315.
1246 doi: 10.1016/j.lithos.2007.08.006
- 1247 Plank, T., & Forsyth, D. W. (2016). Thermal structure and melting condi-
1248 tions in the mantle beneath the Basin and Range province from seismol-
1249 ogy and petrology. *Geochem. Geophys. Geosyst.*, *17*, 1312-1338. doi:
1250 10.1002/2015GC006205
- 1251 Porritt, R. W., Allen, R. M., & Pollitz, F. F. (2014). Seismic imaging east of the
1252 Rocky Mountains with USArray. *Earth Planet. Sci. Lett.*, *402*, 16-25. doi: 10
1253 .1016/j.epsl.2013.10.034
- 1254 Portner, D. E., & Hayes, G. P. (2018). Incorporating teleseismic tomography data
1255 into models of upper mantle slab geometry. *Geophys. J. Int.*, *215*(1), 325-332.
1256 doi: 10.1093/gji/ggy279
- 1257 Rader, E., Emry, E., Schmerr, N., Frost, D., Cheng, C., Menard, J., . . . Geist,
1258 D. (2015). Characterization and Petrological Constraints of the Midlitho-
1259 spheric Discontinuity. *Geochem. Geophys. Geosyst.*, *16*, 3484-3504. doi:
1260 10.1002/2015GC005943
- 1261 Ringwood, A. (1975). *Composition and Petrology of the Earth's Mantle*. New York:
1262 McGraw-Hill.
- 1263 Rogers, N. W., Hawkesworth, C. J., & Ormerod, D. S. (1995). Late Cenozoic
1264 basaltic magmatism in the Western Great Basin, California and Nevada. *J.*
1265 *Geophys. Res.*, *100*(B6), 10287-10301. doi: 10.1029/94JB02738

- 1266 Romanowicz, B. A., & Mitchell, B. J. (2015). Deep Earth Structure: Q of the Earth
1267 from Crust to Core. In G. Schubert (Ed.), *Treatise on Geophysics (Second Edi-*
1268 *tion)* (p. 789-827). Elsevier. doi: 10.1016/B978-0-444-53802-4.00021-X
- 1269 Rondenay, S. (2009). Upper Mantle Imaging with Array Recordings of Converted
1270 and Scattered Teleseismic Waves. *Surv. Geophys.*, *30*, 377-405. doi: 10.1007/
1271 s10712-009-9071-5
- 1272 Roth, J. B., Fouch, M. J., James, D. E., & Carlson, R. W. (2008). Threedimen-
1273 sional seismic velocity structure of the northwestern United States. *Geophys.*
1274 *Res. Lett.*, *35*(L15304). doi: 10.1029/2008GL034669
- 1275 Rowe, M. C., Peate, D. W., & Newbrough, A. (2011). Compositional and thermal
1276 evolution of olivine-hosted melt inclusions in small-volume basaltic eruptions:
1277 a “simple” example from Dotsero Volcano, NW Colorado. *Contrib. Mineral.*
1278 *Petrol.*, *161*, 197-211. doi: 10.1007/s00410-010-0526-y
- 1279 Rychert, C. A., Rondenay, S., & Fischer, K. M. (2007). P-to-S and S-to-P imaging
1280 of a sharp lithosphereasthenosphere boundary beneath eastern North America.
1281 *J. Geophys. Res.*, *112*(B08314), 1-21. doi: 10.1029/2006JB004619
- 1282 Rychert, C. A., & Shearer, P. M. (2009). A Global View of the Lithosphere-
1283 Asthenosphere Boundary. *Science*, *324*(5926), 495-498. doi: 10.1126/
1284 science.1169754
- 1285 Savage, B., & Silver, P. G. (2008). Evidence for a compositional boundary within
1286 the lithospheric mantle beneath the Kalahari craton from S receiver functions.
1287 *Earth Planet. Sci. Lett.*, *272*, 600-609. doi: 10.1016/j.epsl.2008.05.026
- 1288 Schaeffer, A., & Lebedev, S. (2014). Imaging the North American continent using
1289 waveform inversion of global and USArray data. *Earth Planet. Sci. Lett.*, *402*,
1290 26-41. doi: 10.1016/j.epsl.2014.05.014
- 1291 Schmandt, B., & Humphreys, E. (2010). Complex subduction and small-scale
1292 convection revealed by body-wave tomography of the western United States
1293 upper mantle. *Earth Planet. Sci. Lett.*, *297*, 435-445. doi: 10.1016/
1294 j.epsl.2010.06.047
- 1295 Schmandt, B., & Humphreys, E. (2011). Seismically imaged relict slab from the 55
1296 Ma Siletzia accretion to the northwest United States. *Geology*, *39*(2), 175-178.
1297 doi: 10.1130/G31558.1
- 1298 Schmandt, B., & Lin, F.-C. (2014). P and S wave tomography of the mantle be-
1299 neath the United States. *Geophys. Res. Lett.*, *41*, 6342-6349. doi: 10.1002/
1300 2014GL061231
- 1301 Schmandt, B., Lin, F.-C., & Karlstrom, K. E. (2015). Distinct crustal isostasy
1302 trends east and west of the Rocky Mountain Front. *Geophys. Res. Lett.*, *42*,
1303 10290-10298. doi: 10.1002/2015GL066593
- 1304 Schmidt, M. E., Grunder, A. L., & Rowe, M. L. (2008). Segmentation of
1305 the Cascade Arc as indicated by Sr and Nd isotopic variation among di-
1306 verse primitive basalts. *Earth Planet. Sci. Lett.*, *266*(1-2), 166-181. doi:
1307 10.1016/j.epsl.2007.11.013
- 1308 Schulze, K., Marquardt, H., Kawazoe, T., Ballaran, T. B., McCammon, C.,
1309 Koch-Müller, M., ... Marquardt, K. (2018). Seismically invisible wa-
1310 ter in Earth’s transition zone? *Earth Planet. Sci. Lett.*, *498*, 9-16. doi:
1311 10.1016/j.epsl.2018.06.021
- 1312 Selway, K., Ford, H., & Kelemen, P. (2015). The seismic mid-lithosphere discontinu-
1313 ity. *Earth Planet. Sci. Lett.*, *414*, 45-57. doi: 10.1016/j.epsl.2014.12.029
- 1314 Shen, W., & Ritzwoller, M. H. (2016). Crustal and uppermost mantle structure be-
1315 neath the United States. *J. Geophys. Res.: Solid Earth*, *121*, 4306-4342. doi:
1316 10.1002/2016JB012887
- 1317 Shen, X., Kim, Y., Song, T.-R. A., & Lim, H. (2019). Data-oriented constraint on
1318 the interpretation of S receiver function and its application to observations of
1319 seismic discontinuities in the lithosphereasthenosphere system. *Geophys. J.*
1320 *Int.*, *219*, 496-513. doi: 10.1093/gji/ggz316

- 1321 Sigloch, K. (2011). Mantle provinces under North America from multifrequency P
1322 wave tomography. *Geochem. Geophys. Geosyst.*, *12*(2), 1-27. doi: 10.1029/
1323 2010GC003421
- 1324 Simmons, N. A., Forte, A. M., Boschi, L., & Grand, S. P. (2010). GyPSuM: A
1325 joint tomographic model of mantle density and seismic wave speeds. *J. Geo-*
1326 *phys. Res.*, *115*(B12310). doi: 10.1029/2010JB007631
- 1327 Smith, E. I., Sánchez, A., Walker, J. D., & Wang, K. (1999). Geochemistry of Mafic
1328 Magmas in the Hurricane Volcanic Field, Utah: Implications for Small and
1329 LargeScale Chemical Variability of the Lithospheric Mantle. *J. Geol.*, *107*(4),
1330 433-448. doi: 10.1086/314355
- 1331 Smyth, J. R. (1987). β - Mg₂SiO₄: A potential host for water in the mantle?
1332 *Am. Mineral.*, *72*, 1051-1055.
- 1333 Sodoudi, F., Yuan, X., Kind, R., Lebedev, S., Adam, J. M. C., Kästle, E., &
1334 Tilmann, F. (2013). Seismic evidence for stratification in composition and
1335 anisotropic fabric within the thick lithosphere of Kalahari Craton. *Geochem.*
1336 *Geophys. Geosyst.*, *14*, 5393-5412. doi: 10.1002/2013GC004955
- 1337 Sodoudi, F., Yuan, X., Liu, Q., Kind, R., & Chen, J. (2006). Lithospheric thickness
1338 beneath the Dabie Shan, central eastern China from S receiver functions. *Geo-*
1339 *phys. J. Int.*, *166*, 1363-1367. doi: 10.1111/j.1365-246X.2006.03080.x
- 1340 Sonder, L. J., & Jones, C. H. (1999). Western United States Extension: How the
1341 West was Widened. *Annu. Rev. Earth Planet.*, *27*(1), 417-462. doi: 10.1146/
1342 annurev.earth.27.1.417
- 1343 Song, T.-R. A., Helmberger, D. V., & Grand, S. P. (2004). Low-velocity zone atop
1344 the 410-km seismic discontinuity in the northwestern United States. *Nature*,
1345 *427*, 530-533. doi: 10.1038/nature02231
- 1346 Spetzler, J., & Snieder, R. (2004). The Fresnel volume and transmitted waves. *Geo-*
1347 *physics*, *69*(3), 653-663. doi: 10.1190/1.1759451
- 1348 Stein, S., Stein, C. A., Elling, R., Kley, J., Keller, G. R., Wysession, M., ...
1349 Moucha, R. (2015). Insights from North America's failed Midcontinent
1350 Rift into the evolution of continental rifts and passive continental margins.
1351 *Tectonophysics*, *744*, 403-421. doi: 10.1016/j.tecto.2018.07.021
- 1352 Stern, T. A., Henrys, S. A., Okaya, D., Louie, M. K., Savage, S., Lamb, H., ...
1353 Iwasaki, T. (2015). A seismic reflection image for the base of a tectonic plate.
1354 *Nature*, *518*, 85-88. doi: 10.1038/nature14146
- 1355 Stixrude, L., & Lithgow-Bertelloni, C. (2005). Thermodynamics of mantle minerals
1356 - I. Physical properties. *Geophys. J. Int.*, *162*(2), 610-632. doi: 10.1111/j.1365
1357 -246X.2005.02642.x
- 1358 Stixrude, L., & Lithgow-Bertelloni, C. (2011). Thermodynamics of mantle minerals
1359 - II. Phase equilibria. *Geophys. J. Int.*, *184*(3), 1180-1213. doi: 10.1111/j.1365
1360 -246X.2010.04890.x
- 1361 Sundberg, M., & Cooper, R. (2010). A composite viscoelastic model for incorporat-
1362 ing grain boundary sliding and transient diffusion creep; correlating creep and
1363 attenuation responses for materials with a fine grain size. *Philos. Mag.*, *90*(20),
1364 2817-2840. doi: 10.1080/14786431003746656
- 1365 Sweetkind, D. S., Rytuba, J. J., Langenheim, V. E., & Fleck, R. J. (2011). Geology
1366 and geochemistry of volcanic centers within the eastern half of the Sonoma
1367 volcanic field, northern San Francisco Bay region, California. *Geosphere*, *7*(3),
1368 629-657. doi: 10.1130/GES00625.1
- 1369 Tackley, P. J., Xie, S., Nakagawa, T., & Hernlund, J. W. (2005). Numerical and
1370 laboratory studies of mantle convection: Philosophy, accomplishments, and
1371 thermochemical structure and evolution. In R. D. van der Hilst, J. D. Bass,
1372 J. Matas, & J. Trampert (Eds.), *Earth's Deep Mantle: Structure, Composi-*
1373 *tion, and Evolution*. Washington, DC: American Geophysical Union. doi:
1374 10.1029/160GM07
- 1375 Tan, Y., & Helmberger, D. V. (2007). Trans-Pacific upper mantle shear velocity

- 1376 structure. *J. Geophys. Res.*, *112*(B08301), 1-20. doi: 10.1029/2006JB004853
- 1377 Tauxin, B., Debayle, E., & Wittlinger, G. (2008). The mantle transition zone as
1378 seen by global Pds phases: No clear evidence for a thin transition zone beneath
1379 hotspots. *J. Geophys. Res.*, *113*(B08309), 1-17. doi: 10.1029/2007JB005364
- 1380 Tauxin, B., Debayle, E., & Wittlinger, G. (2010). Seismic evidence for a global low-
1381 velocity layer within the Earth's upper mantle. *Nat. Geosci.*, *3*, 718721. doi:
1382 10.1038/ngeo969
- 1383 Tauxin, B., Kim, S., & Kennett, B. L. N. (2017). Pervasive seismic low-
1384 velocity zones within stagnant plates in the mantle transition zone: Ther-
1385 mal or compositional origin? *Earth Planet. Sci. Lett.*, *477*, 1-13. doi:
1386 10.1016/j.epsl.2017.08.006
- 1387 Tauxin, B., van der Hilst, R. D., Wittlinger, G., & Ricard, Y. (2013). Multiple
1388 transition zone seismic discontinuities and low velocity layers below west-
1389 ern United States. *J. Geophys. Res.: Solid Earth*, *118*, 2307-2322. doi:
1390 10.1002/jgrb.50182
- 1391 Thio, V., Cobden, L., & Trampert, J. (2015). Seismic signature of a hydrous man-
1392 tle transition zone. *Phys. Earth Planet. Inter.*, *250*, 46-63. doi: 10.1016/j.pepi
1393 .2015.11.005
- 1394 Toffelmier, D. A., & Tyburczy, J. A. (2007). Electromagnetic detection of a 410-km-
1395 deep melt layer in the southwestern United States. *Nature*, *447*, 991-994. doi:
1396 10.1038/nature05922
- 1397 van der Lee, S., & Frederiksen, A. (2005). Surface Wave tomography applied to
1398 the North American upper mantle. In A. Levander & G. Nolet (Eds.), *Seismic
1399 Earth: Array Analysis of Broadband Seismograms*. doi: 10.1029/157GM05
- 1400 van der Lee, S., & Nolet, G. (1997). Seismic image of the subducted trail-
1401 ing fragments of the Farallon plate. *Nature*, *386*(6622), 266-269. doi:
1402 10.1038/386266a0
- 1403 Vinnik, L., & Farra, V. (2007). Low S velocity atop the 410-km discontinuity and
1404 mantle plumes. *Earth Planet. Sci. Lett.*, *262*, 398-412. doi: 10.1016/j.epsl.2007
1405 .07.051
- 1406 Vinnik, L., Ren, Y., Stutzmann, E., Farra, V., & Kiselev, S. (2010). Observations
1407 of S410p and S350p phases at seismograph stations in California. *J. Geophys.
1408 Res.*, *115*(B05303), 1-12. doi: 10.1029/2009JB006582
- 1409 Vinnik, L. P. (1977). Detection of waves converted from P to SV in the mantle.
1410 *Phys. Earth Planet. Inter.*, *15*(1), 39-45. doi: 10.1016/0031-9201(77)90008-5
- 1411 Vinnik, L. P., Foulger, G. R., & Du, Z. (2005). Seismic boundaries in the mantle
1412 beneath Iceland: a new constraint on temperature. *Geophys. J. Int.*, *160*, 533-
1413 538. doi: 10.1111/j.1365-246X.2005.02529.x
- 1414 Wang, K., Plank, T., Walker, J. D., & Smith, E. I. (2002). A mantle melting pro-
1415 file across the Basin and Range, SW USA. *J. Geophys. Res.*, *107*(B1). doi: 10
1416 .1029/2001JB000209
- 1417 Watt, J. P., Davies, G. F., & O'Connell, R. J. (1976). The elastic properties
1418 of composite materials. *Rev. Geophys.*, *14*(4), 541-563. doi: 10.1029/
1419 RG014i004p00541
- 1420 Weidner, D. J., & Wang, Y. (1998). Chemical- and Clapeyron-induced buoyancy at
1421 the 660 km discontinuity. *J. Geophys. Res.*, *103*(B4), 7431-7441. doi: 10.1029/
1422 97JB03511
- 1423 Wenrich, K. J., Billingsley, G. H., & Blackerby, B. A. (1995). Spatial migra-
1424 tion and compositional changes of Miocene-Quaternary magmatism in the
1425 Western Grand Canyon. *J. Geophys. Res.*, *100*(B6), 10417-10440. doi:
1426 10.1029/95JB00373
- 1427 Whitmeyer, S. J., & Karlstrom, K. E. (2007). Tectonic model for the Proterozoic
1428 growth of North America. *Geosphere*, *3*, 220-259. doi: 10.1029/2012JB009639
- 1429 Williams, H., Hoffman, P. F., Lewry, J. F., Monger, J. W. H., & Rivers, T. (1991).
1430 Anatomy of North America: thematic geologic portrayals of the continent.

- 1431 *Tectonophysics*, 187(1-3), 117-134. doi: 10.1016/0040-1951(91)90416-P
- 1432 Wilson, D. C., Angus, D. A., Ni, J. F., & Grand, S. P. (2006). Constraints on the in-
1433 terpretation of S-to-P receiver functions. *Geophys. J. Int.*, 165, 969-980. doi:
1434 10.1111/j.1365-246X.2006.02981.x
- 1435 Wölbern, I., Rümpker, G., Link, K., & Sodoudi, F. (2012). Melt infiltration of the
1436 lower lithosphere beneath the Tanzania craton and the Albertine rift inferred
1437 from S receiver functions. *Geochem. Geophys. Geosyst.*, 13(8), 1-20. doi:
1438 10.1029/2012GC004167
- 1439 Wood, B. J., & Holloway, J. R. (1984). A thermodynamic model for subsolidus equi-
1440 libria in the system CaOMgOAl₂O₃SiO₂. *Geochim. Cosmochim. Acta*, 48(1),
1441 159-176. doi: 10.1016/0016-7037(84)90358-2
- 1442 Xiao, J., Hier-Majumder, S., Tauzin, B., & Waltham, D. (2020). An inversion
1443 approach for analysing the physical properties of a seismic low-velocity
1444 layer in the upper mantle. *Phys. Earth Planet. Inter.*, 304(106502). doi:
1445 10.1016/j.pepi.2020.106502
- 1446 Xu, W., Lithgow-Bertelloni, C., Stixrude, L., & Ritsema, J. (2008). The effect of
1447 bulk composition and temperature on mantle seismic structure. *Earth Planet.*
1448 *Sci. Lett.*, 275, 70-79. doi: 10.1016/j.epsl.2008.08.012
- 1449 Yogodzinski, G. M., Naumann, T. R., Smith, E. I., & Bradshaw, T. K. (1996).
1450 Evolution of a mafic volcanic field in the central Great basin, south Central
1451 Nevada. *J. Geophys. Res.*, 101(B8), 17425-17445. doi: 10.1029/96JB00816
- 1452 Yuan, H., French, S., Cupillard, P., & Romanowicz, B. (2014). Lithospheric
1453 expression of geological units in central and eastern North America from
1454 full waveform tomography. *Earth Planet. Sci. Lett.*, 402, 176-186. doi:
1455 10.1016/j.epsl.2013.11.057
- 1456 Yuan, H., & Romanowicz, B. (2010). Lithospheric layering in the North American
1457 craton. *Nature*, 466(7310), 1063-1068. doi: 10.1038/nature09332
- 1458 Yuan, H., Romanowicz, B., Fischer, K. M., & Abt, D. (2011). 3-D shear wave
1459 radially and azimuthally anisotropic velocity model of the North Ameri-
1460 can upper mantle. *Geophys. J. Int.*, 184(3), 1237-1260. doi: 10.1111/
1461 j.1365-246X.2010.04901.x
- 1462 Yuan, X., Kind, R., Li, X., & Wang, R. (2006). The S receiver functions: synthet-
1463 ics and data example. *Geophys. J. Int.*, 165, 555-564. doi: 10.1111/j.1365-246X
1464 .2006.02885.x
- 1465 Zhang, Q., Sandvol, E., & Liu, M. (2009). Lithospheric velocity structure of the New
1466 Madrid Seismic Zone: A joint teleseismic and local P tomographic study. *Geo-*
1467 *phys. Res. Lett.*, 36(L11305). doi: 10.1029/2009GL037687

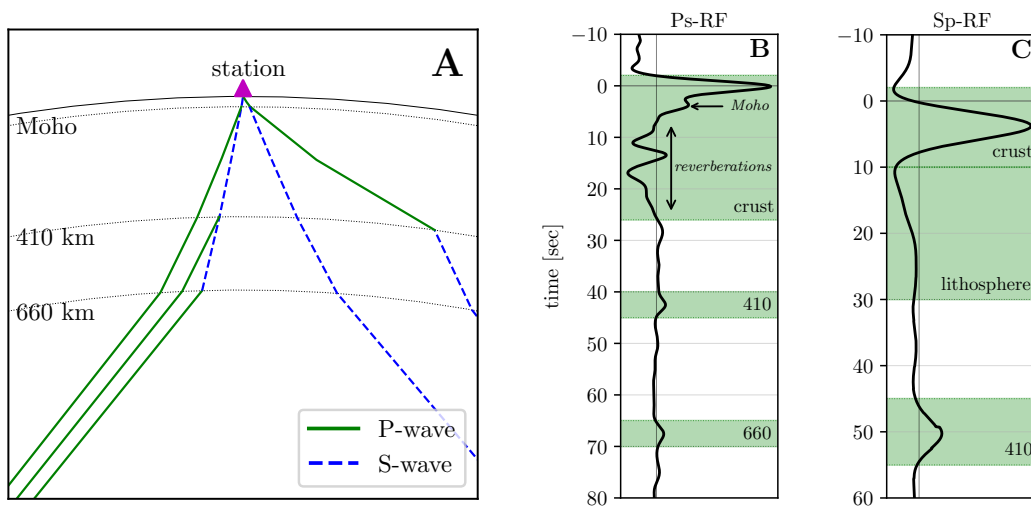


Figure 1. Illustration of conversions of body waves at the Moho and the 410- and 660-km seismic discontinuities in the Earth (A) and corresponding synthetic P-to-s (B) and S-to-p receiver functions (C) based on the seismic reference model IASP91 (Kennett & Engdahl, 1991). P- and S-waves are shown as green (solid) and blue (dashed) lines, respectively. Time windows including arrivals of converted waves are shaded in green. Note that the polarity and time axis of Sp RFs are flipped as a result of which arrivals with positive travel times arrive prior to the S-wave and are not masked by crustal reverberations as is the case for P-to-s conversions

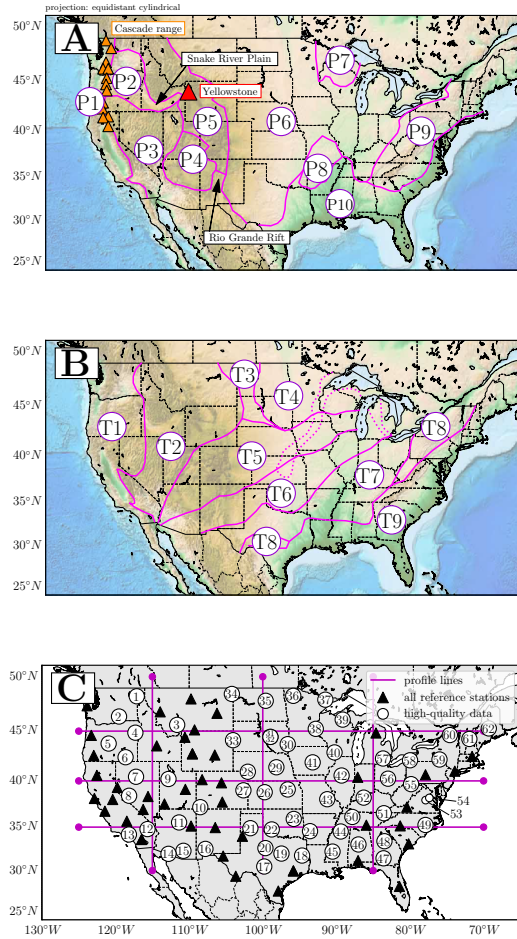


Figure 2. Main physiographic features (Fenneman, 1928) of the contiguous USA (**A**): P1: Pacific mountain system (incl. Cascade Range); P2: Columbia plateau (incl. Snake River Plain and Yellowstone Hotspot); P3: Basin and Range (incl. Rio Grande Rift); P4: Colorado plateau; P5: Rocky mountain system; P6: Interior Highlands; P7: Laurentian Highlands; P8: Interior Highlands; P9: Appalachian Highlands; P10: Atlantic Plain. The tectonic provinces (Hoffman, 1988; Whitmeyer & Karlstrom, 2007) represent the long-term geological history of the continent **B**: the oldest parts of the continent, i.e., of precambrian age, include the Greater Wyoming province (T2) and Superior craton (T4), which are connected along the Trans-Hudson orogen (T3). Proterozoic orogenies accreted the Yavapai (T5), Mazatzal (T6), Granite-Rhyolite (T7), and Grenville provinces (T8) to the cratonic core. During episodes of extension in proterozoic times, the mid-continental rift was formed but abandoned, and later the Pacific and paleo-Atlantic oceans were opened. The closure of the latter during the paleozoic formed the Appalachian mountain belt (T9, P9), which, nowadays, is bordered by the Atlantic plains (P10), i.e., the relatively young passive continental margin, to the east and south. In contrast to the east, the western margin (T1) is dominated by subduction processes acting since the mesozoic (e.g., Sonder & Jones, 1999; Dickinson, 2004; Humphreys, 2009), which have resulted in accretion of terrane to the American continent, volcanism (Cascade range, P1), and extensional tectonics (Basin and Range, P3). The topography model underlying the maps is that of ETOPO1 (Amante & Eakins, 2009). **C**: location of USArray reference stations (www.usarray.org). White circles indicate stations, where either P-to-s or S-to-p receiver functions or both were inverted, while black triangles represent stations for which data were processed but because of quality constraints were not considered in the inversion. Station numbering and details are given in Table S.1. Magenta lines indicate profiles along which cross sections of mantle seismic properties are shown

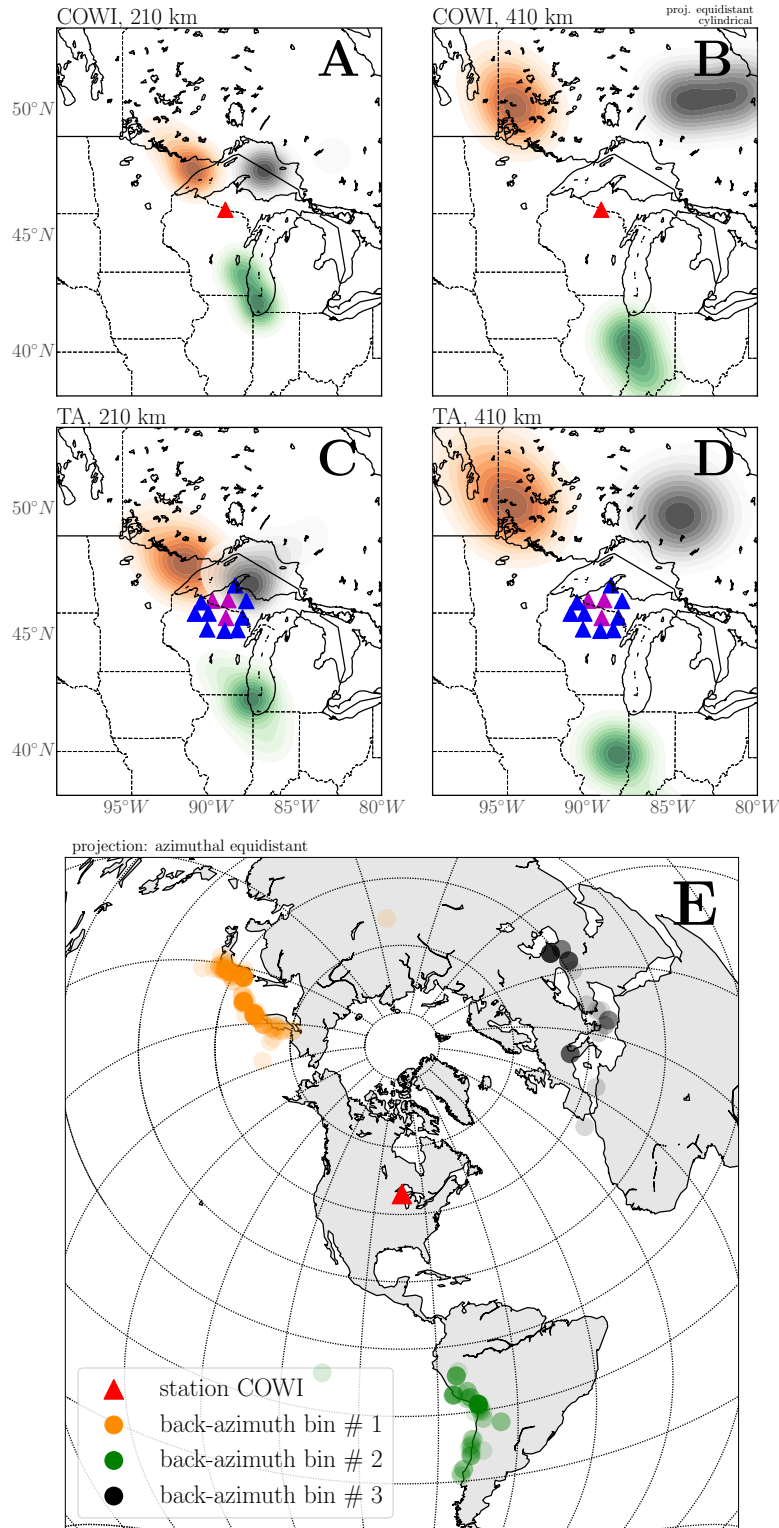


Figure 3. A–D: normalized Fresnel-zone weights of S-to-p piercing points (color coded by back-azimuth; see panel E) at a depth of 210 km (A and C) and 410 km (B and D) for the events recorded at 39-COWI (red triangle) and 12 near-by transportable USArray stations within a distance of ~ 70 km (TA1; magenta triangles) and ~ 140 km (TA2; blue triangles), respectively. E: location of station 39-COWI and the seismic events used for computing S-to-p receiver functions coloured by back-azimuth (dots)

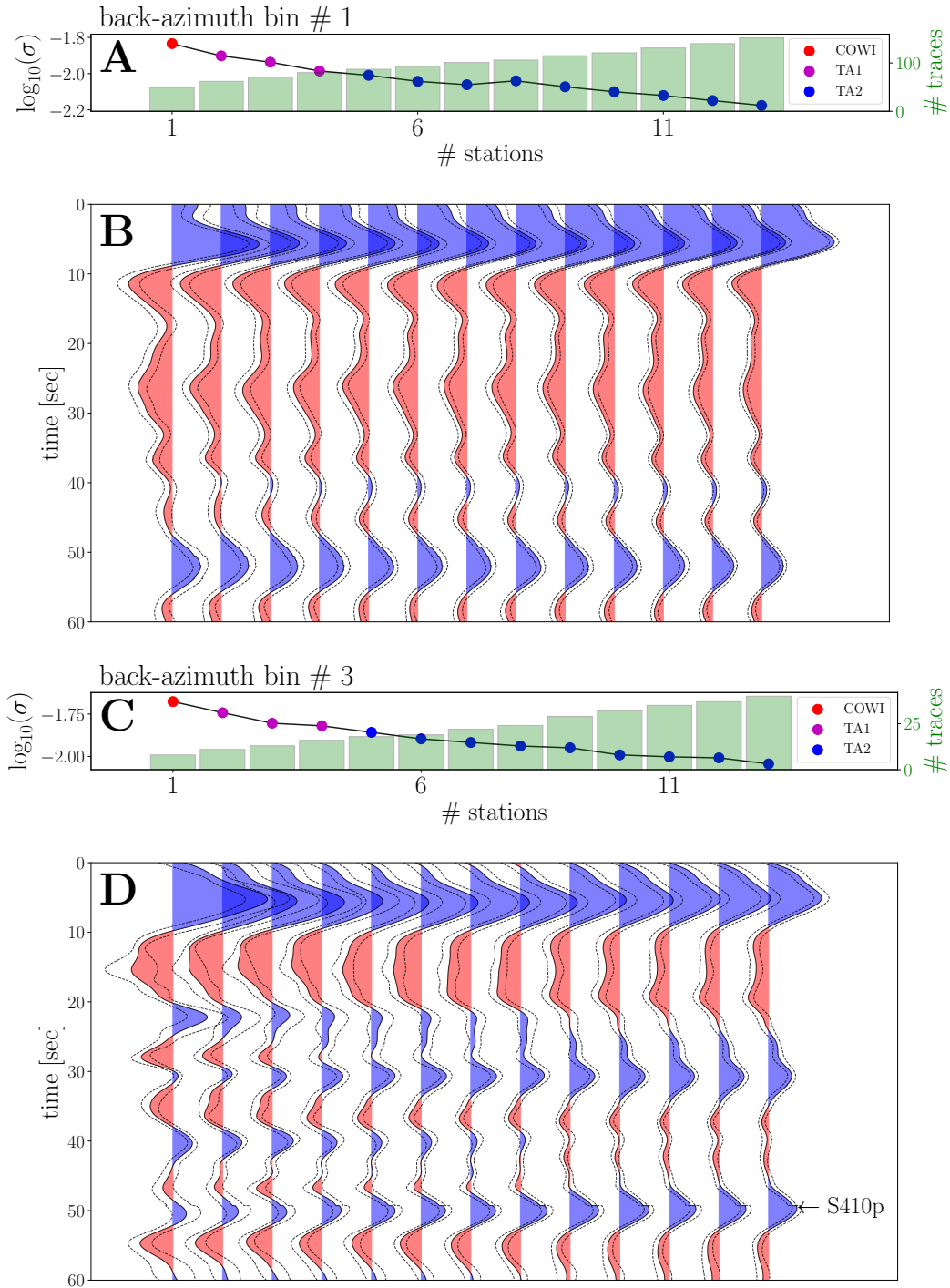


Figure 4. S-to-p receiver function stacks, mean uncertainty (σ), and number of summed traces (green bars) for two distinct back-azimuth bins related to events in the west Pacific (#1; **A** and **B**) and Europe (#3; **C** and **D**), respectively. Including data recorded at transportable stations (blue and magenta dots) (TA1 and TA2, respectively) of the reference station (39-COWI, red dot) reduces uncertainty and enhances the S410p phase in back-azimuth bin # 3 (**D**)

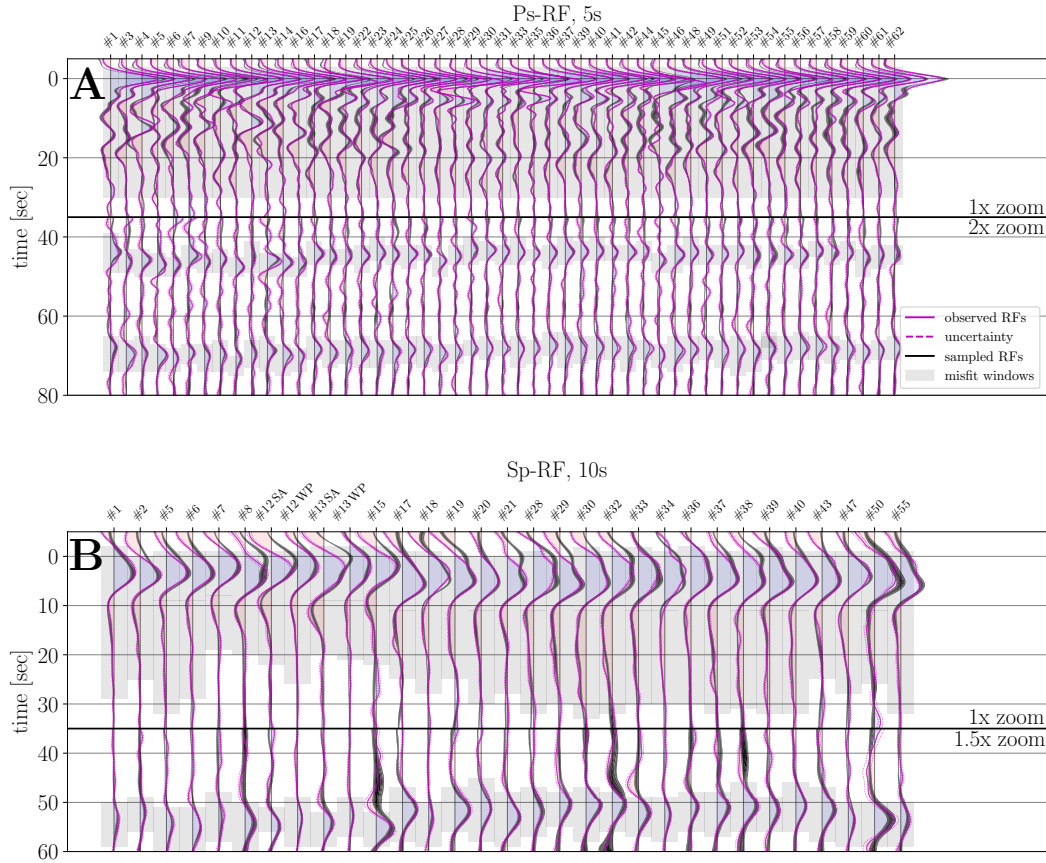


Figure 5. Data misfit between inverted and observed high-quality P-to-s (5 s low-pass period, **A**) and S-to-p receiver functions (10 s low-pass period, **B**). Observations and uncertainties are shown as magenta lines, sampled receiver functions as contours (dark bands), and misfit windows in light gray. Station numbering is shown in Figure 2C, whereas ‘SA’ and ‘WP’ denote events located in South America and the West Pacific, respectively. For improved visibility, amplitudes of conversions from the 410- and 660-km seismic discontinuities have been scaled up. Equivalent data fits for P-to-s and S-to-p receiver functions at low-pass periods of 8, 10, and 15 s are shown in supplementary Figure S.19

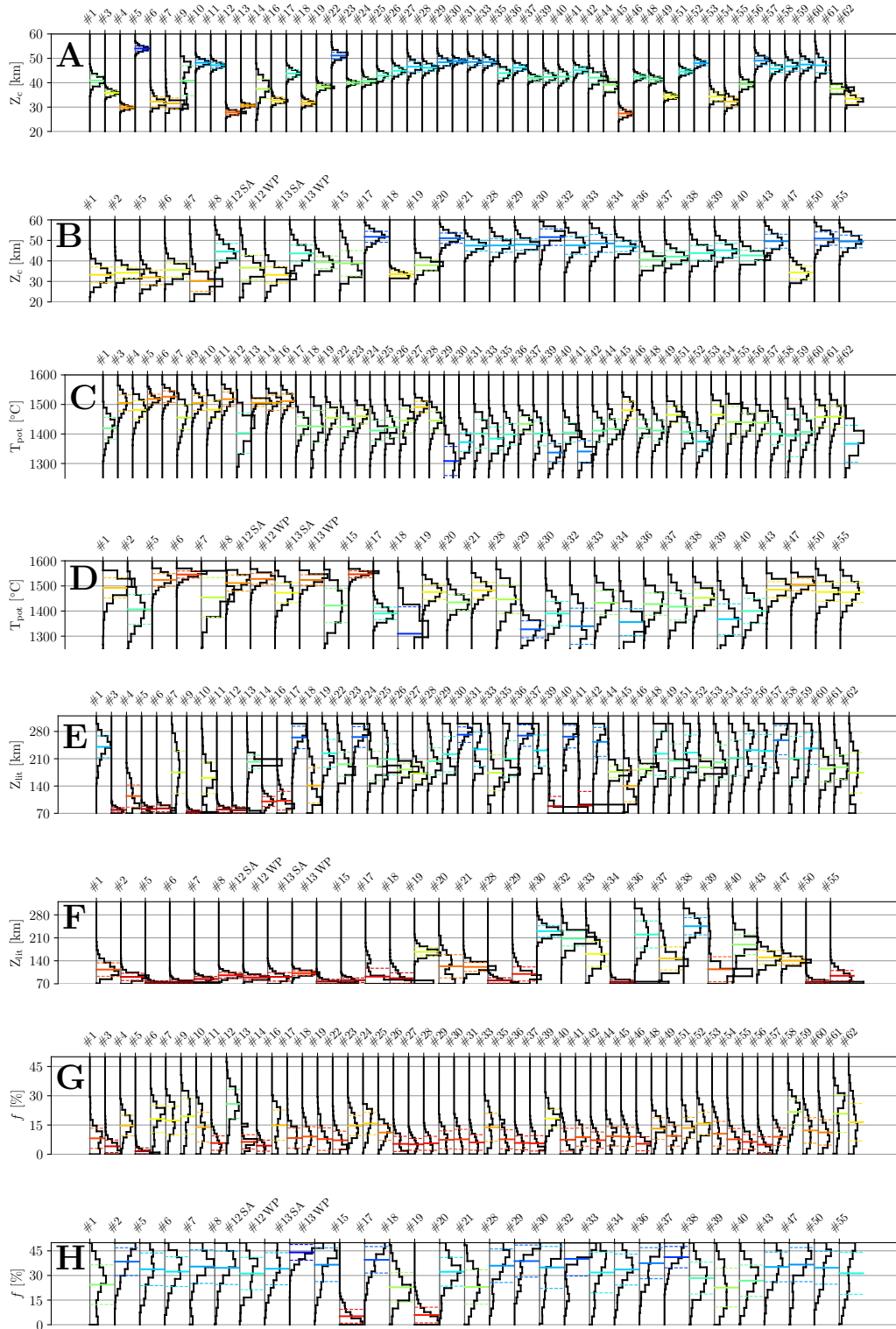


Figure 6. Sampled marginal posterior probability distributions (black lines) of crustal thickness, Z_c (A, B), potential temperature, T_{pot} (C, D), lithosphere thickness, Z_{lit} (E, F), and basalt fraction, f (G, H) from inversion of P-to-s and S-to-p receiver functions, respectively. Mean values and standard deviations of the distributions are shown as thick and thin lines, respectively, where choice of color is based on the colormaps used in Figures 7 and 9. Station numbering refers to Figure 2C, whereas ‘SA’ and ‘WP’ refer to events from South America and the West Pacific, respectively

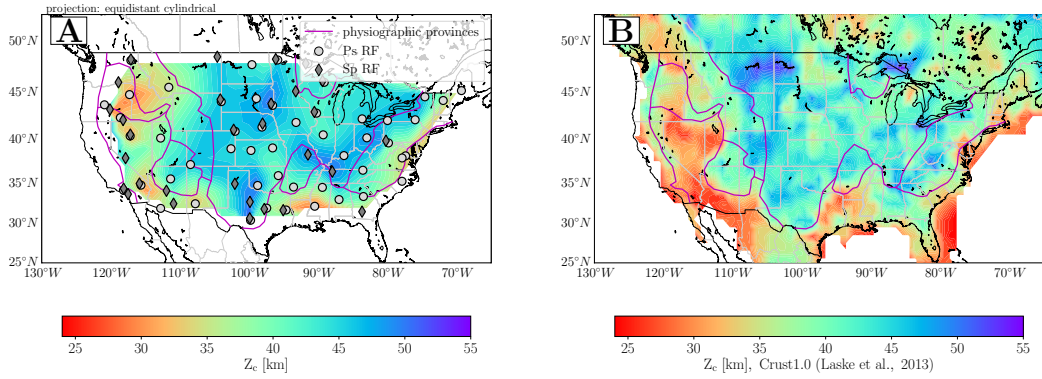


Figure 7. **A:** Mean crustal thickness, Z_c , across the contiguous USA interpolated from migrated P-to-s (circles) and S-to-p (diamonds) receiver functions. **B:** Crustal thickness map from model Crust1.0 (Laske et al., 2013). Physiographic provinces are outlined in magenta (Fenneman, 1928, cf. Figure 2A)

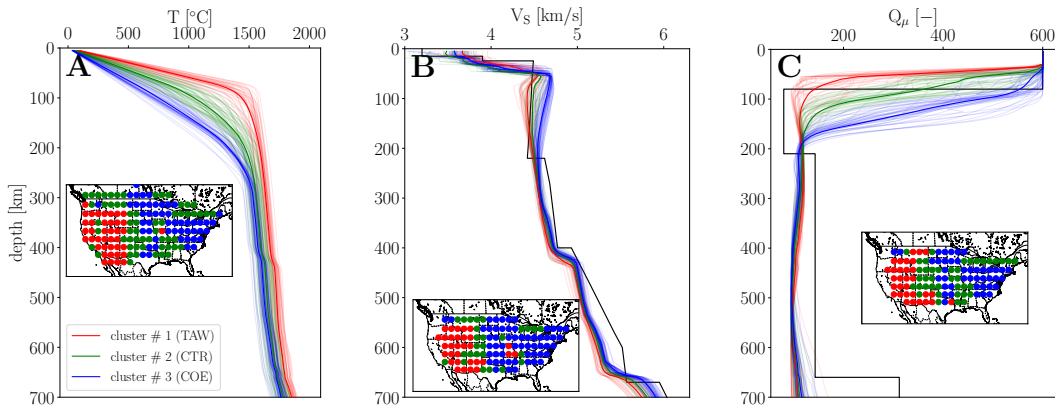


Figure 8. Profiles of temperature (T , **A**), S-wave velocity (V_s , **B**), and shear attenuation profiles (Q_μ , **C**) obtained from inversion of P-to-s and S-to-p receiver functions and clustering analysis. Profiles are clustered into three clusters according to similarity (color-coded) and displayed in light color, whereas the mean profile of each cluster is shown as a thick line. The tectonic regions identified in panel **A** will be referred to as tectonically active West (red; TAW), central transition regions (green; CTR), and cratonic-orogenic East (blue; COE) in the following. The maps shown in the insets are interpolated from the inversion results on a $2.5^\circ \times 2.5^\circ$ -grid. PREM profiles are shown in black in panels (**B**) and (**C**)

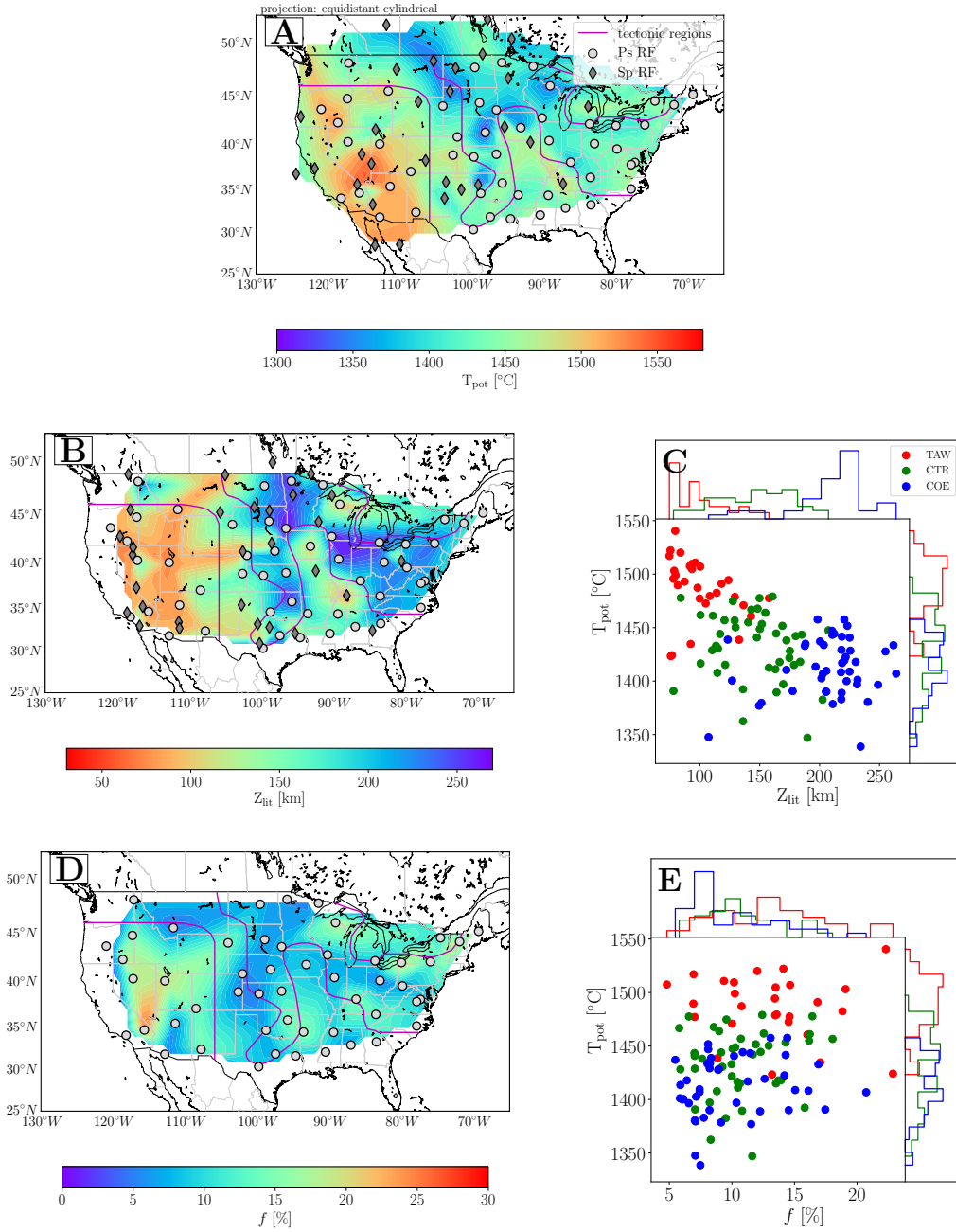


Figure 9. Models of the North American thermo-chemical mantle structure: potential temperature, T_{pot} (A), lithosphere thickness, Z_{lit} (B), and basalt fraction, f (D). Tectonic regions identified earlier (cf. Figure 8A) are outlined in magenta. The distribution and correlation of T_{pot} with Z_{lit} and f for each of these tectonic regions (color coded) are shown in panels C and E, respectively. Maps derive from P-to-s (circles) and S-to-p (diamonds) receiver functions, respectively, except the compositional map showing basalt fraction (D), where S-to-p receiver function estimates are excluded because of the large uncertainties (see section 6.6). Differences in lateral extent of these maps arise from the migration of S-to-p receiver function results along the converted raypath to different depths (see section 5.4)

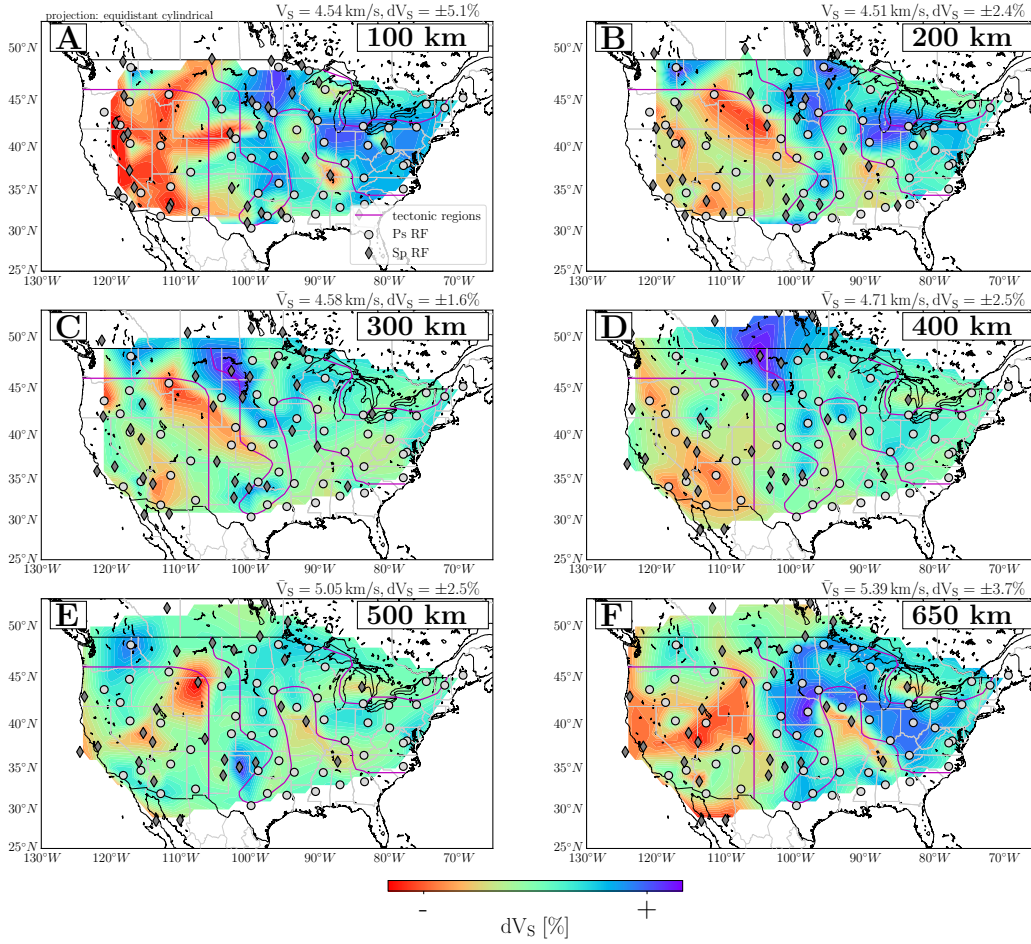


Figure 10. Interpolated S-wave velocity perturbations, dV_S , along horizontal slices between 100–650 km depth. All maps share the same colormap but differ in absolute mean velocity and standard deviation (indicated on the top right of each panel). Earlier identified tectonic regions (cf. Figure 8A) are outlined in magenta. Differences in lateral extent of these maps arise from the migration of S-to-p receiver function results along the converted raypath to different depths (see section 5.4)

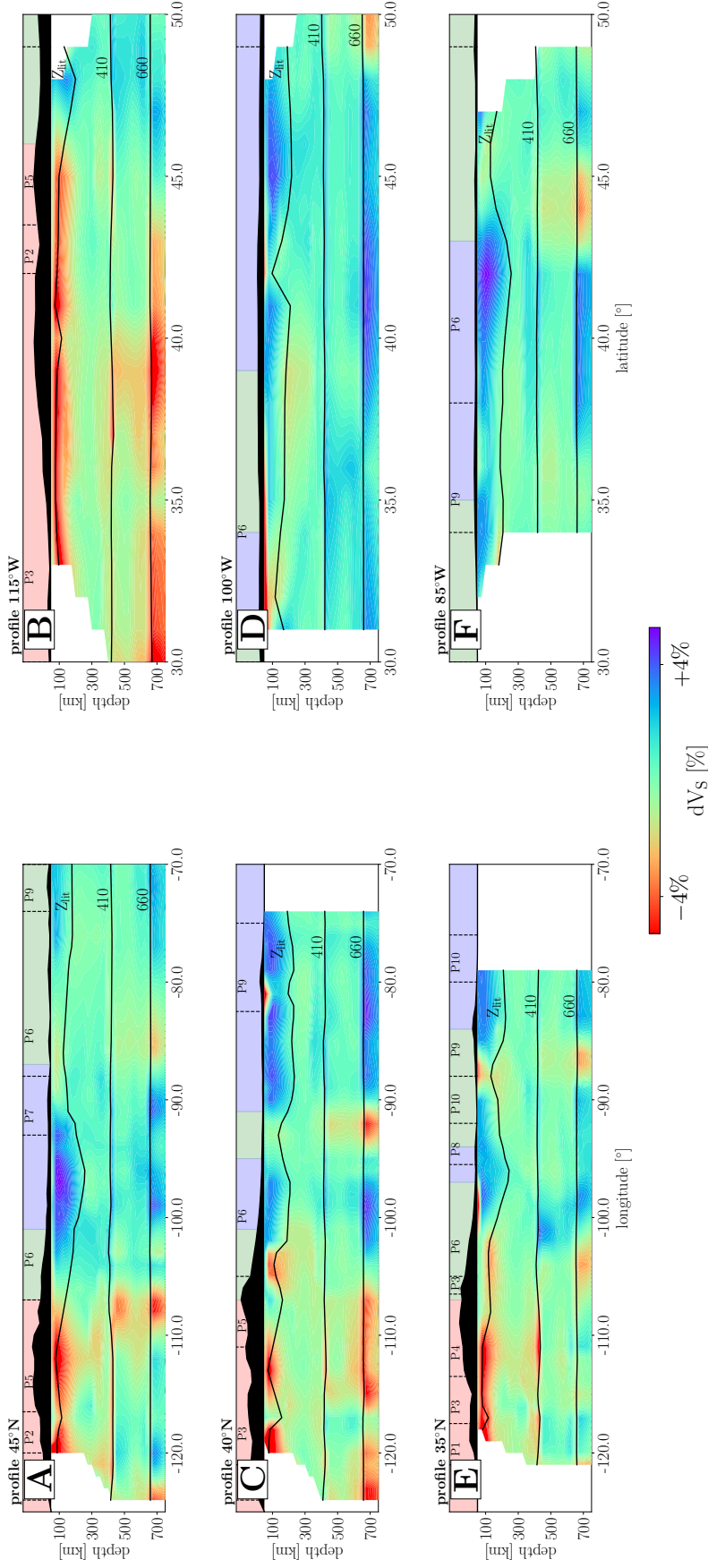


Figure 11. Longitudinal cross sections of S-wave velocity perturbations (**A**, **C**, and **E**) at 45°N, 40°N, and 35°N latitude, respectively, and latitudinal cross sections (**B**, **D**, and **F**) at 115°W, 100°W, and 85°W longitude, respectively. Lines indicating location of cross sections are shown in Figure 2C. The perturbation is computed relative to the mean velocity with depth (not shown). Surface topography (Laske et al., 2013) is exaggerated 50× and black lines represent topography on lithosphere and 410- and 660-km seismic discontinuities. Differences in lateral extent with depth arise from the migration of S-to-p receiver functions along the converted raypath to different depths (see section 5.4). Above each panel, the extent of the tectonic regions identified in Figure 8A are indicated by different colors: TAW (red), CTR (green), and COE (blue). Physiographic provinces (Fenneman, 1928, cf. Figure 2A) are outlined with dashed vertical lines

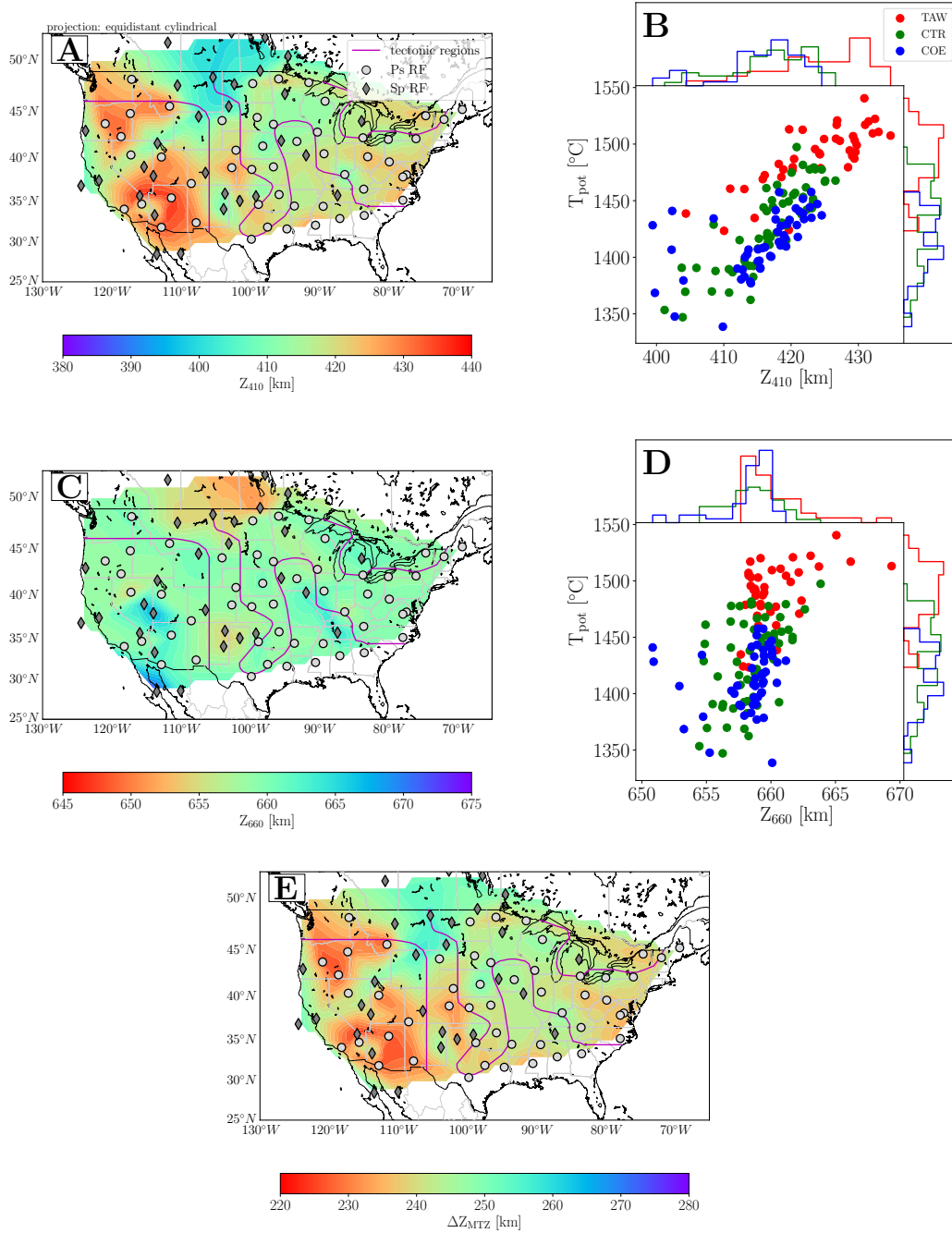


Figure 12. Interpolated maps of mean depth to the major mantle seismic discontinuities at 410 and 660 km depth, Z_{410} (A), Z_{660} (C), and mantle transition zone thickness, ΔZ_{MTZ} (E). Tectonic regions identified in Figure 8A are outlined in magenta. The distribution and correlation of mantle potential temperature T_{pot} with Z_{410} and Z_{660} for each of these regions (color coded) is shown in panels B and D, respectively

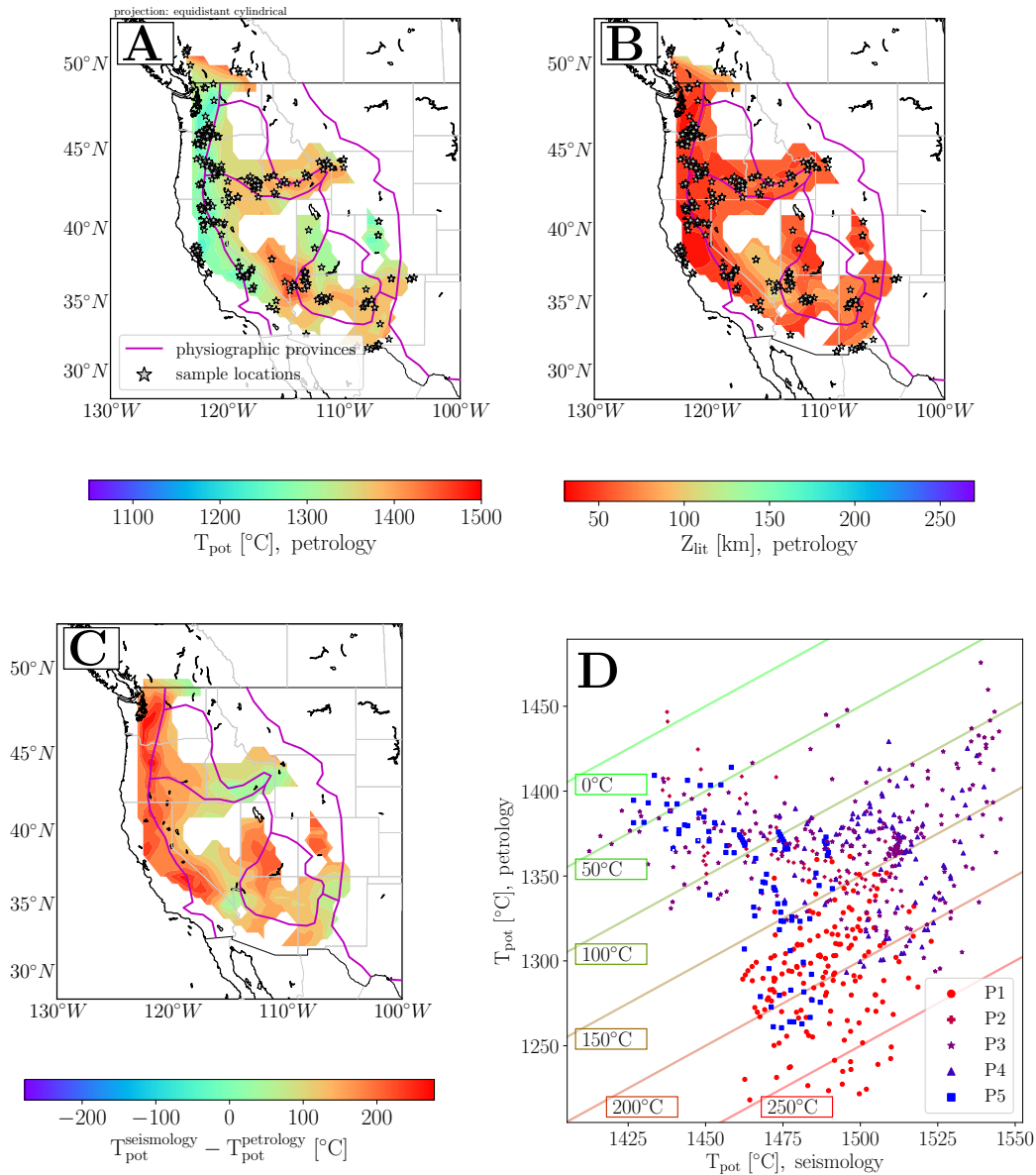


Figure 13. Thermo-chemical structure of the lithosphere underneath the western USA as estimated from thermobarometry: interpolated potential temperature (T_{pot} , **A**) and lithosphere thickness (Z_{lit} , **B**). The deviation to seismically derived temperature estimates (cf. Figure 9A) is shown in panel **C**. Cells of the interpolation grid farther away than 1.5° from the nearest sample location (stars) are masked. Physiographic provinces are outlined in magenta (Fenneman, 1928, cf. Figure 2A). Panel **D** compares the petrologically and seismically derived temperature estimates (markers colored by physiographic province). Isotherms represent absolute temperature differences, i.e., $T_{\text{pot}}(\text{seismology}) - T_{\text{pot}}(\text{petrology})$ (color coded and labeled)